FAILURE PREDICTION AND STRESS ANALYSIS OF MICROCUTTING TOOLS

A Thesis

by

SUJEEV CHITTIPOLU

Submitted to the Office of Graduate Studies of
Texas A&M University
in partial fulfillment of the requirements for the degree of

MASTER OF SCIENCE

May 2009

Major Subject: Mechanical Engineering

FAILURE PREDICTION AND STRESS ANALYSIS OF MICROCUTTING TOOLS

A Thesis

by

SUJEEV CHITTIPOLU

Submitted to the Office of Graduate Studies of
Texas A&M University
in partial fulfillment of the requirements for the degree of

MASTER OF SCIENCE

Approved by:

Chair of Committee,	Wayne N. P. Hung
Committee Members,	Chii-Der Suh
	Terry Creasy
Head of Department,	Dennis L. O’Neal

May 2009

Major Subject: Mechanical Engineering

ABSTRACT

Failure Prediction and Stress Analysis of Microcutting Tools. (May 2009)

Sujeev Chittipolu, B.E., Osmania University, India

Chair of Advisory Committee: Dr. Wayne N. P. Hung

Miniaturized devices are the key producing next-generation microelectro-mechanical products. The applications extend to many fields that demand high-level tolerances from microproducts and component functional and structural integrity. Silicon-based products are limited because silicon is brittle. Products can be made from other engineering materials and need to be machined in microscale.

This research deals with predicting microtool failure by studying spindle runout and tool deflection effects on the tool, and by measuring the cutting force that would fail the tool during microend-milling. End-milling was performed using a tungsten carbide (Ø1.016 mm dia., 2 flute) tool on SS-316L material.

Tool runout, measured using a laser, was found to be less than 1 µm and tool deflection at 25000 rpm was 20 µm. Finite element analysis (FEA) predicts tool failure due to static bending for a deflection greater than 99% of tool diameter. Threshold values of chipload and cutting force resulting in tool failure were found using workdone by tool. Threshold values to predict tool failure were suggested for axial depth of cut in between 17.25% -

34.5% of cutter length. For a chipload greater than 20% of cutter diameter, the microtool fails instantly for any radial depth of cut.

ACKNOWLEDGEMENTS

This material is based upon work supported by the National Science Foundation under grant No. 0552885. I would like to thank my advisor, Dr. Hung, for providing an outstanding research environment. The completion of this project would not have been possible without the patience, invaluable advice and guidance provided by Dr. Hung during the course of my research. I would also like to thank my committee members, Dr. Creasy and Dr. Suh, for their guidance and support throughout the course of this research.

I would like to thank my colleague, Saurabh Kajaria, in HAAS CNC Lab for helping me throughout the work. Thanks also go to my friends and the department faculty and staff for making my time at Texas A&M University a great experience.

I would like to thank our sponsor, Haas Automation Inc., MA Ford and UNIST Inc. for their generous support without which the project would not have materialized.

Finally, thanks to my mother and father for their love, encouragement and numerous sacrifices. Sincere thanks to my brother, sister and brother-in-law for their support.

TABLE OF CONTENTS

LIST OF FIGURES

FIGURE Page

FIGURE Page

LIST OF TABLES

LIST OF SYMBOLS

α	End rake angle
β	Friction angle
ϵ_f	Strain in the outer surface of beam
μ	Coefficient of friction
ϕ	Shear plane angle
σ_f	Stress in outer fibers at midpoint of beam subjected to flexure test
τ	Shear strength of work piece material
θ_1	Included angle between x- axis and line 1
θ_2	Included angle of the arc made by cutting tool
A	Shear area of chip
A_f	Friction area
A_{r1}	The additional area due to runout in feed direction
A_{r2}	The additional area due to runout in the direction perpendicular to feed
b	Length along the edge of work piece where the tool fails
D	Maximum deflection of the center of the beam
e	Tool with runout
E	Modulus of elasticity in bending
f_c	Chip load or feed per tooth
F_c	Cutting force in the direction of feed
F_p	Principle cutting force responsible for the power consumed
F_s	Shearing force along the shear plane

h	Axial depth of cut
I	Section inertia moment of wire, for circular cross section
l	Arc length of the circle 1 between line 1 and x- axis
L	Support span of beam subjected to flexure test
P	Load at a given point on the load deflection curve
R	Radius of cutting tool
t	Undeformed chip thickness
u	Specific energy of workpiece material
w	Width of cut or radial depth of cut
x	x- coordinate of intersection of line1 and circle 1
X	Feed direction coordinate
Y	Normal direction coordinate

1. INTRODUCTION

The market trend for product miniaturization requires research and education in micromanufacturing. Micromachining removes chips in micro/nano scales. Micromachining requires special equipment and new tooling for success. Common techniques for macro scale machining often lead to inconclusive data when applied to micromachining.

Having achieved a strong technical competence during the several years of remarkable technological development, it is appropriate to consider the future needs of production engineering from the cutting technologies perspective. Cutting technology is multidisciplinary with economics playing an increasingly important role. The key change drivers for cutting technology include diminished component size, enhancing surface quality, tightening tolerances and accuracies, reducing costs and diminishing component weight. The curves presented by Taniguchi (1983) and updated by McKeown (1987) in Figure 1 trace the development in manufacturing capability in terms of achievable machining accuracy. Today, precision machine tools under computer control, using single point or multipoint cutting tools, can position the tool relative to the workpiece to a resolution and position accuracy of 1nm. Figure 2 shows micromachining relative to other processes such as EDM,

---

This thesis follows the style of *Journal of Manufacturing Systems*.

grinding, laser machining, and silicon etching technologies. The figure also shows that surface roughness can be only 5nm for features up to 1 µm using micromachining.

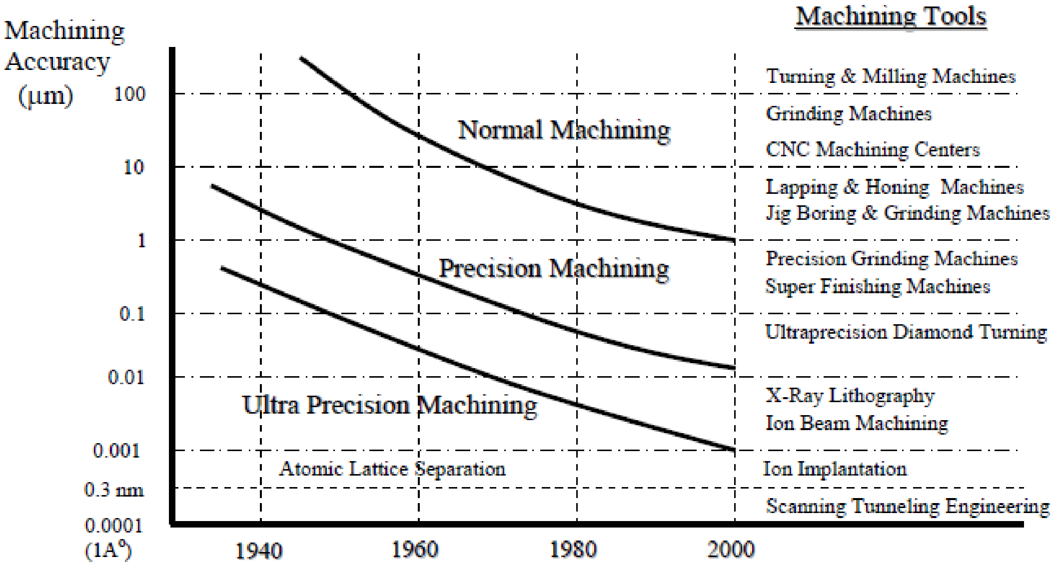

Figure 1. The development of achievable machining accuracy (McKeown 1987)

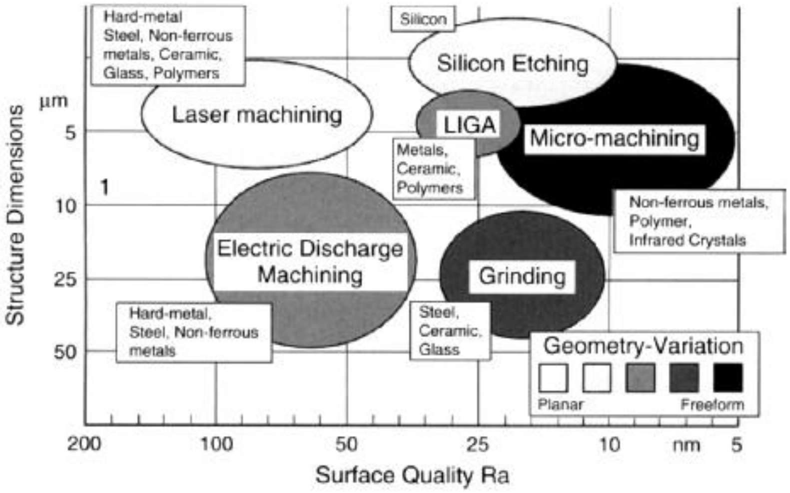

Figure 2. Micromachining relative to other machining process (Byrne et al. 2003)

Micromachining is key to manufacturing of many advanced microelectro-mechanical products for many industrial and medical applications. The continuous demand for increased functionality, reduced size and small complex features in large components has increased research for micromachining technologies. The current non-conventional machining processes used for micromachining suffer from several inherent problems: high cost equipment, toxic chemicals, limited selection in workpiece material and inability to build complex 3D components with high aspect ratio. On the other hand, the tool based manufacturing processes like micromilling, microEDM, microgrinding, and etc., can create various three dimensional structures owing to easily defined tool paths applicable to many materials while simultaneously maintaining high accuracies in terms of tolerance to feature size. These advantages led to the increased demand to apply conventional micromachining techniques to microscale components.

Micromilling is versatile machining process which is considered to be an attractive alternative for micromanufacturing due to its high flexibility of the process and the ability to produce complex 3-D features. Micromilling is not a miniature version of conventional milling. In fact, there are fundamental differences between the processes: different chip formation mechanisms, cutting forces, surface roughness, and machining dynamics. In micromachining higher feeds relative to that in conventional machining would result in high stress in tools. Such high stress generated would drastically reduce tool life of the microtool and sometimes result in tool failure. Typical microtool diameters vary from 0.1 mm to 1 mm. The size and life of microcutting tools determines the accuracy and economics involved in micromachined features. Microtools have been of prime interest because premature tool failure and unpredictable tool life disrupt the machining process. In micromachining process it is difficult to identify tool failure during machining; failure results in a lost machining if the broken tool is not detected before the machining is finished. In addition, once the tool fails on a workpiece, the work piece is often discarded because inspection and resetting is very time consuming.

A lot of research was done to study tool failure and factors involved in it. Many approaches were followed; the research studied cutting conditions, system dynamics, cutting forces, tool wear, tool geometry, and etc. Most approaches were based on empirical models that neglect several important factors and involve complex numerical algorithms. This project proposes a new approach: measure the tool runout and maximum cutting force acting on the tool. The tool runout in micromilling is highly significant and accurate measure of tool runout is an important factor to understand the micromachining process. Cutting force was measured in the feed direction using a novel end-milling experiment that was analyzed with a mathematical cutting force model based on shear area of cut. This mathematical model can be executed much faster than existing complex iterative algorithms to predict the cutting force. The cutting force acting on the tool during machining was also estimated using the specific energy of the workpiece material. Finite element analysis (FEA) technique was also used to analyze the effect of cutting force on microtool. The finite element analysis technique gives an advantage to extend the tool failure study to different cutting conditions.

1.1. RESEARCH OBJECTIVES

The main objectives of the research would be:

1. Predict microtool failure due to spindle runout.
2. Predict microtool failure due to cutting force.
3. Apply FEA technique to predict the tool failure for different conditions of tool deflection and cutting force.

1.2. RESEARCH SCOPE

The scope of this research is limited to microend-milling using a 2-flute tungsten carbide cutter on 316L stainless steel. Micromist is used as cutting fluid in this study.

2. LITERATURE REVIEW

The terms micro- and nanotechnology are, these days, typically used to describe the components, phenomena and applications related to very small dimensions to the range of a few hundred microns. Micromachining is the most basic technology used in the production of advanced miniaturized parts and components (Taniguchi 1983). Miniaturization of devices is a key to the production of next generations of several kinds of microelectro-mechanical products for a wide variety of fields that include electronics, biotechnology, medical applications, optics, military, communications, and avionics, to name a few (Masuzawa 2000). The level of applications in all the above fields demand very high tolerances of microcomponents, and both functional and structural requirements demand the use of various engineering materials, including stainless steel, titanium, brass, aluminum, platinum, iridium, plastics, ceramics, and composites (Liu et al. 2004).

The two basic groups of micromachining process are mask based and tool based micromachining. The mask based technology or non-conventional technology uses the method of applying a thin film using several different deposition techniques, applying lithographic techniques to apply mask material, etching to get the desired microscale features, using chemical or plasma etching to remove the mask material, then finally the created microstructures are separated from the substrate material. Other techniques used in mask based micromachining include fusion bonding or using vacuum techniques to bond a thin coating to the substrate. The applications such as diesel injection nozzle, microelectrode and miniature tuning fork are produced by non-conventional micromachining methods. Microcomponents like micro bevel gears, microimplants are produced by DUV (deep ultraviolet lithography) method. Several MEMS (microelectro-mechanical systems) devices are made using the manufacturing techniques used in for the semiconductor industry like the wet etching, plasma etching, LIGA, etc., The other non-conventional micromachining methods also include laser beam machining, electron beam machining where thermal energy is used to do the machining of components. The nontraditional fabrication methods are cost effective only in bulk machining due to the high initial cost and poor productivity (Masuzawa et al. 1997).

Though these machining process have several applications, these technologies suffer from several limitations that encumber the use of these methods to address the specific needs (Liu et al. 2004). First and foremost these methods are generally used on silicon and silicon like materials and have limitations of fabricating 3D structures as they are applied to only two dimensional planar shapes. On the other hand the tool based manufacturing processes are capable of creating various three dimensional structures owing to the easily defined tool path and the clear border at the tool – work piece surface (Masuzawa 2000). And the solid tools can be used on a wide range of materials and maintain relative accuracies for tolerance-to-feature size in the range of 10^{-3} to 10^{-5} range unlike the mask based micromachining process where the relative accuracies are in the order of 10^{-1} to 10^{-2} (Liu et al. 2004). Considering several advantages lot of research has been done to develop flexible and effective technologies for the production of microcomponents.

The tool based micromachining as discussed has an advantage of fabricating complex features with high accuracy on a wide range of materials. These mechanical micromachining can be done either by designing ultra precision machine tools and cutting tools, like ultra precision diamond turning machines, or by designing miniature versions of the machine tools like the micro-lathe, micromill etc. The machining using microend-milling process is fast and also cost efficient as compared to other processes. For the micro-features of sizes up to 5 μm, low surface roughness, high accuracy and high material removal rates can be achieved using microend-milling with the recent development in the miniature machine tools (Uhlmann 2005). Though micromachining incorporates several ideas of conventional machining, several issues and challenges are raised due to the size and scale of manufacturing.

2.1 MICROMACHINING

Micromilling has been considered to be an attractive alternative for micromanufacturing due to its high flexibility of the process and the ability to produce complex three-dimensional features (Newby 2005). The first step towards micromachining not using the conventional machining techniques was done by Higuchi and Yamagata in 1993. The initial work was mainly focused on developing the microcutting tools for micromachining. A microtool of 25 micron diameter was fabricated as an experiment to produce microtools by scaling down the conventional techniques within micrometer tolerances. The tool geometry of the microtool showed a variation from its actual scaled-down version of its macroscopic counterpart (Vasile et al., 1996). The next stage of research was on developing miniaturized machine tools. A micro-lathe system of 32 mm in length was fabricated by Kitahara et al. in 1996. The system suffered from a poor accuracy and limited capabilities in shape generation. Improving the first design Lu et al. (1999) developed and analyzed a micro-lathe turning system. This system had a maximum dimension of 200 mm in length, with a spindle speed of up to 15,000 rpm and was provided with a dynamometer to study the cutting forces during machining. The work piece was 0.3 mm in diameter and cutting was done using a diamond single point tool. This micro-lathe could create components like micro-screws of 120 micron diameter but the surface roughness was comparable to conventional lathes, which was accounted to low cutting speeds of about 3m/min.

Several studies were performed which had a significant contribution in developing the fundamental understanding of micromilling process. Several factors like the size effect, cutting force, minimum chip thickness, chipload, cutting speeds and feeds, surface roughness, cutter runout, cutting temperature, tool life, multiphase materials, microstructure effects etc., were extensively studied to gain the fundamental understanding of the process. For example, the influence of minimum chip thickness effect on surface roughness in micromilling was accounted to material properties as it was found that softer material state during cutting increased the surface roughness

(Weule et al. 2001). Experiments conducted by Kim et al. (2004) showed that chip is not formed with each pass of cutting at lower feed rates by measuring the chip volume to the nominal chip volume and also by examining the distance between feed marks on the machined surface.

2.2 MICROTOOLS

Microtools in end milling are of high priority. The diameters of the cutting tools in micromilling vary from 0.1 mm to 1 mm. The study on microtools was of prime interest in the field of micromilling because of premature tool failure and unpredictable tool life which are of serious concern. Lot of research was done to study the tool failure and several factors involved in it. Many approaches were followed based on the objective of the research to improve the tool life by studying cutting conditions, system dynamics, cutting forces, tool geometry etc.

Use of analytical tools for the design of better cutter tools was started in 1975 by Tlusty and Macneil. Numerical tools were highly used to understand the dynamics of micromilling and to study the influence of runout and tool flexibility (Gu et al. 1991). Several tool failure mechanisms of the microtools in micromilling of aluminum, graphite electrodes and steel were studied. “Tool wear” was redefined as any microscopic change in the tool from its initial state. The changes may be the loss of material during cutting, adhesion of workpiece particles on cutting tool faces, changes in the geometry of the cutting tool after machining etc. In the conventional milling tools wear results in the breakage of cutting edge whereas for the microtools the tools tip completely fails as the tool worn out or if any chip clogs on tool. Small changes in the cutting edge of the microtool may result in the tool failure as loss of material would drastically increase the force thereby proportionately increasing the stress at the shaft of the microtool (Tansel et al. 1998).

Tool failure in microtools is very quick and is difficult to predict ahead. The failure in microdrills due to chip clogging is due to the generation of high stresses which are beyond the endurance limit of the cutting tool. (Konig et al. 1992). Failure of the tool will occur very quickly if the cutting force increases beyond the strength of the tool. As the cutting force increases during the cutting, the workpiece starts to push the shaft of the tool and it deflects. The deflection of the tool and the stress will increase with every rotation. The static component of the force in the direction of feed will increase continuously till the tool breaks. The main reason for the breakage in this case is the excessive stress beyond the endurance limit of the tool (Tansel et al. 1998). The slight changes in cutting force characteristics and tool vibration signals were monitored in microdrilling operation before the tool failure. The study was extended to predict the tool failure by monitoring the static component of feed direction cutting force through use of segmental averages and wavelet transformations in microend-milling by Tansel et al. (1997). The failure was predicted when the static part of feed direction force increases three or four times while the cutting conditions are the same. Figure 3 shows the changes in the cutting force during machining. The increase in cutting force helps to predict the tool failure.

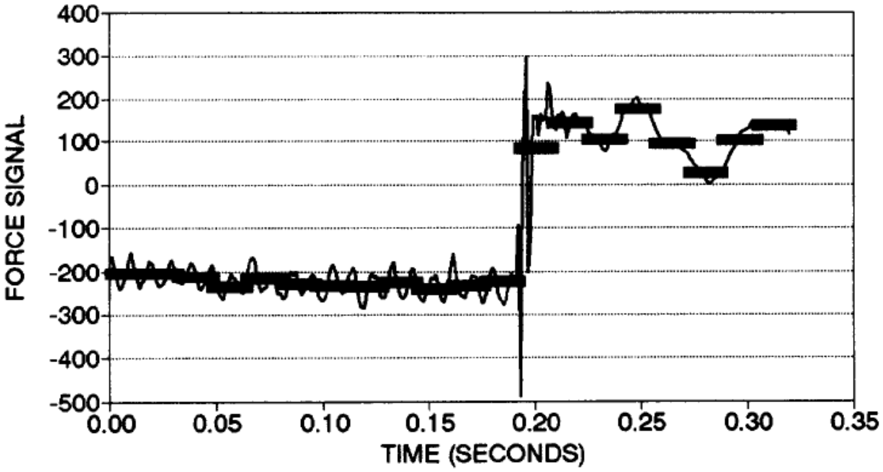

Figure 3. Sample of cutting force data and waveform presented just before and after tool breakage (Tansel 2008)

Effect of tool geometry on tool failure was also extensively studied. Microtools with larger diameter last for a longer time than microtools with relatively smaller diameter under same cutting conditions (Fang et al. 2003). They showed that two flute end mills with diameter of 0.1 mm break very easily compared to same type of end mills with diameter of 0.2 mm. The chipping of tool tip occurs at lower values of cutting force before the cutting tool breaks at the end of the cutter length for a cutting force greater than the rupture strength of the tool. The authors suggested that for cutter diameters of 0.1 mm the D-type end mills have higher rigidity and cutting performance than helical end mills, but the applications of the semi-circle based end mills are very limited compared to helical end-mills.

Tool runout is caused by imperfect tool alignment, asymmetric tool geometry, mismatch between tool and machine tool, and vibration of tools during machining (Stephenson, and Agapiou 1997). Figure 4 shows the affect of cutter runout on the size of a machined slot. In addition, radial cutting forces deflect cutting tools like a cantilever beam. For a conventional macro-scale machining process, the run-out, typically on the order of micrometers, has a negligible effect on the dimensional accuracy of the machined feature. For micromachining, however, the tool run-out to tool diameter ratio becomes much larger.

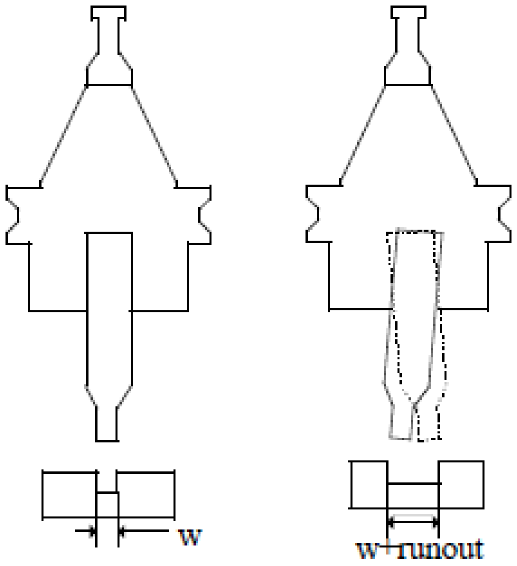

Figure 4. Comparison of ideal channel and channel machined with runout (Lee et al. 2004)

Several theoretical models were developed and justified to measure the tool runout in micromilling process. Effect of runout on the force variations is highly negligible in conventional milling process compared to the micromilling process. The presence of cutter runout in micromilling would sometimes cause one of the cutting edge of two flute end mill to perform machining while the other edge not performing any cutting operation. This would result in high force variations in the microtool and high tool wear in one flute which would increase the probability of tool failure. Estimation of cutter runout in micromilling was performed from the force expression developed, considering the trochoidal trajectory of the tool and angle between the tool cutting edge and tool rotation axis by Bao et al. (2000a).

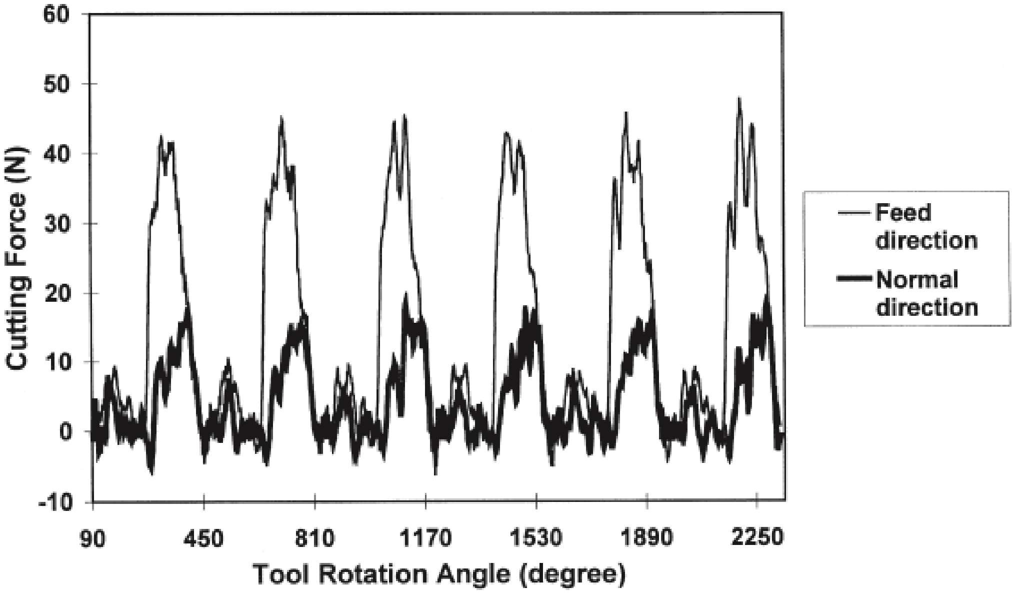

Figure 5. Experimental cutting force signals of microend-milling with tool runout. (Bao et al. 2000a)

Figure 5 shows the cutting force data obtained when machining EDM POCO-3 graphite workpiece using a 0.02" diameter two flute HSS end-mill. The cutting conditions of 15,000 rpm spindle speed, 20 ipm to 120 ipm feed rate, 0.01" to 0.05" width of cut and 0.01" axial depth of cut were maintained. The runout was estimated by inspecting the difference of peaks of the cutting force data. According to their test results, run-outs of the holder with a collet were 0% to 65% and runouts of the conventional holder were between 40% and 87%. Figures 6 and 7 show the trajectory of the two-flute tool tip of microend-milling with a 0º and 90º angles respectively. According to the simulations by Bao et al. (2000b) of microend-milling with tool run-out, the cutting force variation of a two flute end-mill reaches to its maximum when the offset line is parallel to the tool cutting edge and force variation decreases to its minimum if the offset line is perpendicular to the cutting edge.

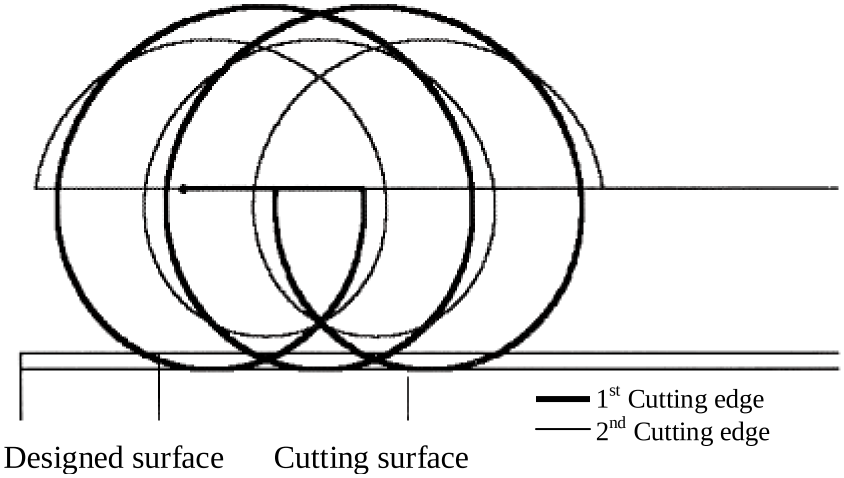

Figure 6. Trajectory of the two-flute tool tip of microend-milling with 0º angle (Bao et al. 2000b)

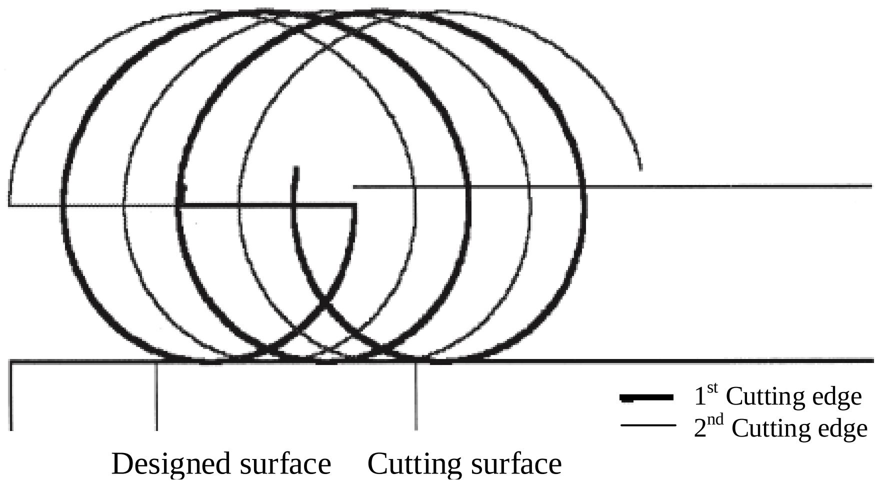

Figure 7. Trajectory of the two-flute tool tip of microend-milling with 90º angle (Bao et al. 2000b)

The force model developed by Li et al. (2004) for conventional end milling accounted for the cutter runout but the magnitude of the cutter runout was measured offline when the spindle is in static state. All the current methods used to calculate the cutter runout are not measured under dynamic spindle/tool motion during the actual cutting process. They are estimated under static conditions of the system and used for research. The runout of the cutter under dynamic conditions and that under static conditions is significantly different and cannot be ignored for the scale at which micromilling is done. The cutter runout at microlevel is influenced by the integrity of the system, spindle speed and also by several external conditions. It is very important to understand and measure the actual cutter runout and its influence on the cutting tool to have an in-depth understanding of the micromachining process.

2.3 CUTTING FORCE

Selection of proper cutting conditions is an important factor in micromachining to ensure a high machining quality and prevent unpredictable failure of microtools. So prediction and precise estimation of cutting forces is of fundamental importance to establish optimization of the machining process. Several models were developed to predict the cutting forces and to understand the factors like the vibrations, process stability, surface texture, cutter runout, shear area etc. These force models can be broadly classified into mechanistic, empirical and analytical models.

An analytical model was proposed by Tlusty et al. (1975) for the cutting forces in conventional end milling considering the circular tool path and constant proportional ratio between chip load and cutting force. Kline et al. (1983) studied the effects of cutter runout on cutting geometry and its effects on cutting forces. The later analytical models tried to calculate the effect of different cutting conditions, up and down milling, total cutting angle, cutting force coefficient etc., on machining (Bao et al. 2000a). Analytical models develop the physical mechanisms during cutting but increasing complex factors like the temperature gradients, multiphase cutting materials, high strain rates, plastic deformations, coolant flow etc., would make it difficult to completely characterize the experimental condition. On the other hand for the empirical models the performance measures like the cutting forces, tool wear, tool life, surface roughness etc., are measured by running several experiments at different cutting conditions (Newby et al.

2005).The basic mechanistic force model was developed by Koenigsberger et al. (1961) assumes a linear relation between the cutting force and chip thickness and estimated the proportionality constant as a factor of cutting conditions and workpiece material. Several mechanistic models were later developed following the Koenigsberger method. A theoretical cutting force model for conventional end milling with helical cutter with runout was modeled by Li et al. (2004). The model analyses the theory of stress distributions along the shear plane and tool-chip interface and estimates the shear angle at which the resultant forces transmitted by shear plane and interface are in equilibrium. The cutting forces were estimated by dividing the helical cutter into small axial slices and integrating the sum of forces on each tooth segment at every slice. A new method to calculate the cutting forces in conventional milling was calculated by Kim et al. (2005) by dynamically measuring the frequencies from the spindle displacement using a cylindrical capacitive displacement sensor (CCDS). This method uses a non-contact magnetic exciter and a displacement sensor to excite the spindle and simultaneously record the displacements of the spindle during cutting. The authors proposed a method to extract the displacement signals related only to cutting out of the total signals received by using the magnetic exciter.

The use of cutting force models for conventional end milling to microend-milling have only resulted with limited success. The ratio of tool runout to tool diameter is comparatively very large in micromilling than conventional end milling process. This phenomenological difference cannot be accounted by scaling down the conventional milling process to micromilling. Also the effect of the edge radius needs to be accounted in micromilling as it is highly significant. The sharpness of the microtool cannot be improved proportional to the decrease of tool size because of the tool fabrication methods employed, which results in chipload very closely comparable to the edge radius (Li et al. 2007).

Several force models were developed to calculate the cutting forces during the micromilling process. Most of the models are based on the concept that chip thickness during machining is proportional to the cutting force. A chip thickness computation algorithm was modeled by Volger et al. (2004) to develop a cutting force model and suggested use of two force models to account for situations when chip is and is not formed during micromachining. A force model for microend-milling was developed by Bao et al. (2000b) considering the trochoidal nature of the tool path and assumed that the tangential cutting force is proportional to the cutting area and the radial cutting force is proportional to the tangential cutting force. The developed cutting force model studied the effects of cutter runout and tool wear on cutting force. The conventional force model developed can be used for chip load to tool radius ratio less than 0.1 and the model has a 15% error in maximum cutting force for the ratio greater than 0.1. Figure 8 shows the cutting force plot obtained from experiments performed by Bao et al. (2000a) using a 1/8” two flute carbide end-mill on a work piece material made of NAK-55 steel. The cutting conditions of 2,000 rpm spindle speed, 1 ipm feed rate, 1/16” width of cut and 1/16” depth of cut were maintained. The difference between the estimated and experimental maximum cutting forces for the presented case was shown to be less than 5%.

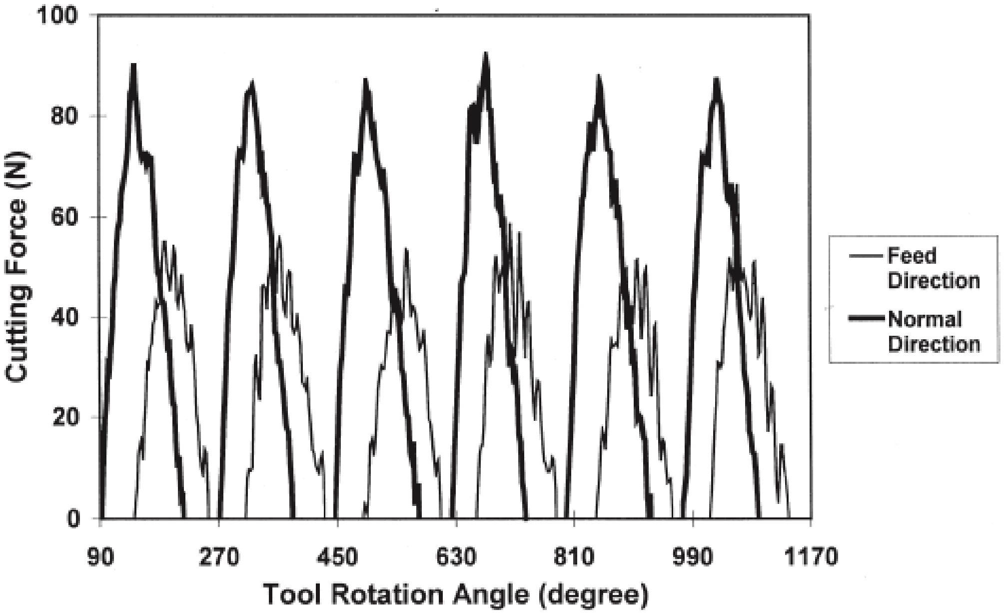

Figure 8. Cutting force plots obtained from micromachining of 3.175 mm (1/8”) carbide end-mill on NAK-55 steel (Bao et al. 2000a)

To enhance the understanding of cutting coefficients or cutting pressure constants in microend-milling Newby et al. (2007) developed an expression for measured forces in cutting, considering the true trochoidal nature of tool path. The authors estimated the cutting constants using the measured cutting forces in the direction of feed and perpendicular to the feed. The empirical equations were produced for cutting constants K_t and K_r. The Figure 9 shows the measured average force in the direction of feed when performing a micromachining using a 800 microns 2 flute carbide end-mill on a 7075-T6 aluminum material. The cutting conditions were maintained at 6200 rpm spindle speed, 0.101 mm feed/tooth and width of cut was varied from 10 to 800 microns.

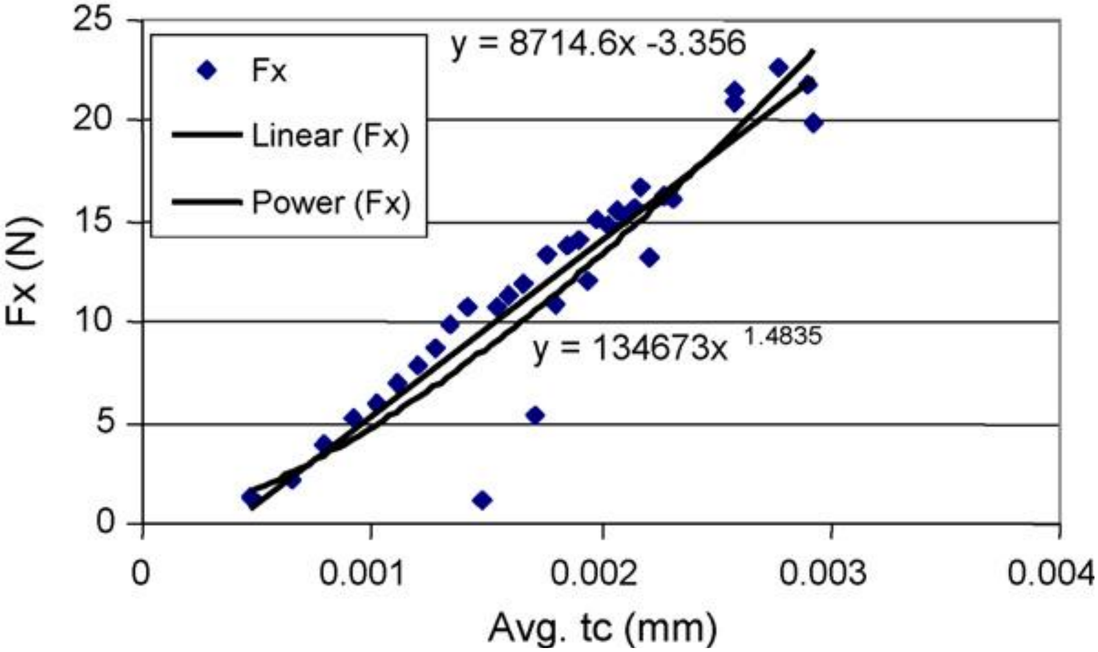

Figure 9. Plot showing cutting force vs average chip thickness for micromachining of 800 micron carbide end-mill on 7075-T6 aluminum material (Newby 2007)

Despite increased sophistication and applications of the force models developed, the predictive capability of force and other predictions highly rely on empirically established force component coefficients for each cutter design (Li et al. 2004).

2.4 APPLICATIONS OF 316L STAINLESS STEEL

Microelectro-mechanical systems (MEMS) were used in various applications such as pressure sensors, biomedical sensors, drug delivery systems, fluid management processing devices etc. in which the fabrication technology was evolved from silicon based integrated circuits techniques. The demands for multiple material microcomponents encourages researchers to develop new fabrication techniques that allow metals, ceramics, alloys, and polymers be used. In terms of good mechanical properties and medical applications, stainless steel components are good materials for these purposes. The 316L stainless steel grade that contains chromium-nickel and molybdenum provides higher resistance to pitting and crevice corrosion in chloride environments. These properties in addition to low carbon contents make it the best candidate for the implanted applications because of the decreasing in vivo corrosion (Ratner 1996). Micrometallic machine components have important applications in the watch-making industry, instrumentation and medical devices and the related fabrication technology has been widely studied. Thus 316L stainless steel alloy is widely used in medicine for applications that include implanted spinal fixation devices, bone screws, cardiovascular and neurological stents, and as critical components of minimally invasive surgical devices (Goodman et al. 2004). These applications are made possible due to suitable physical and mechanical properties, good corrosion resistance in biological environments, reasonable biocompatibility, and good manufacturability. As medical technology advances towards microsurgical and minimally invasive techniques, there is a drive to produce ever-smaller devices that demand higher material performance.

3. EXPERIMENTS

Selecting proper cutting conditions that would increase the tool life is an important factor for any machining process. Considering the weakness of the body of the microtool and the tiny portion of tip involved for cutting, tool failure predictions are highly difficult for microtools. Various parameters can be responsible for the failure of microtools. The parameters like the tool cutting conditions, coolant flow, integrity of system, system dynamics, tool runout, precise positioning of the tool with workpiece all have significant effect on the performance of the tool. Each of it is an extensive area in itself. The current research studies the effect of tool deflection and cutting force on the failure of microtool.

Several experiments were conducted to study the failure of microtools in micromilling. The factors, eccentricity in tool rotation from the axis due to spindle runout and the maximum cutting force on the tool during machining were used to predict the tool failure. Various cutting conditions like the cutting feed, chip load, axial and radial depth of cut, rpm of spindle are used to study the effect of spindle runout and cutting force on tool failure. The experiments were performed using a 1.016 mm two flute carbide end-mill machining on a 316L stainless steel workpiece material. The micromachining system developed by HAAS was used for the experimental work. Positioning the tool with respect to the work piece for machining is also an important aspect for micromachining.

3.1 PROCEDURE

In order to achieve the research objectives, the following tasks were outlined as:

1. Measure the spindle runout using a Keyence displacement laser on a Haas office milling machine (OM2). Runout was measured for different conditions by varying the spindle speeds. Tool deflection was also measured during end milling a straight line cut on a 316L stainless steel using a 1.016 mm diameter carbide end mill. The dynamic tool deflection data while cutting was measured for spindle speeds of 15,000 rpm and 25,000 rpm. The resulting runout data was used to analyze the effect of deflection on the microcutting tool. The maximum tool deflection that would result in tool failure was studied.

2. The cutting force in feed direction acting on the tool that would fail the tool during machining was measured to study the effect of cutting conditions on the microtool. Crash tests were performed to with gradual increase in radial depth of cut to accurately measure the cutting force that would fail the tool. Cutting force was modeled using mathematical model developed on the shear area of cut. Mathematical model was developed to understand the effect of tool runout on friction area and thereby affecting the cutting force.

3. Specific energy for 316L stainless steel was estimated from cutting force data obtained from the crash tests, given the fact that specific energy remains constant for

a given work material operating under different cutting conditions. The cutting force in feed direction was used to estimate the principle cutting force responsible for power and then the specific energy is estimated from it.

4. Finite element analysis was performed to analyze the stress distribution for tool deflections and cutting force. The effect of tool deflection on the tool was extended to see the deflection that would result in the tool fatigue and fracture failure. The maximum cutting force that would fail the cutting tool for different cutting conditions was estimated. The tool failure analysis was extended for cutting force acting on the entire cutter length and as a point load. Also the effect of cutting force on the cutting tool along different cutting angles is measured.

This research predicts microtool failure, therefore reducing time and cost of setup and running.

3.2 EQUIPMENT

3.2.1 M.A. FORD CARBIDE END MILL

All the experiments were done on a 1.016 mm microend-mill provided by M.A. Ford. The tool was a tuff cut 2 flute end mill made of tungsten carbide. The tool cutter diameter was 0.04” or 1.016 mm. The flute length of the cutting tool was 0.08” or 2.032 mm and the shank diameter was equal to 1/8” or 3.175 mm. The helix angle of the cutting flutes was 30^0. Figure 10 below shows the part drawing of the tool.

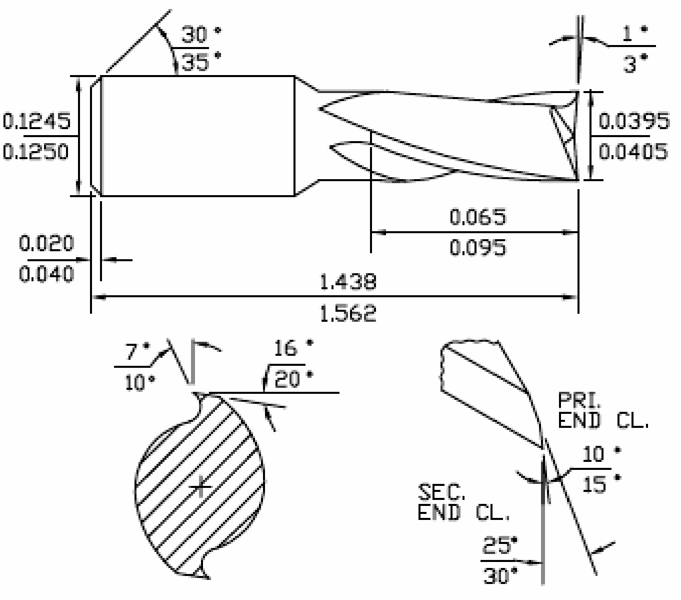

Figure 10. Dimensions of the microend mill (Tool # 1640400 – 0.04x.080x1-1/2) (M.A.Ford 1998)

The specifications of the micro cutting tool and its physical properties are shown in Tables 1 and 2 respectively.

Table 1. Specifications of the tungsten carbide cutting tool (M.A.Ford 1998)

Tool Material	Tungsten carbide
Number of flutes	2
Cutter diameter	1.016 mm
Cutter length	2.032 mm
Shank diameter	3.175 mm

Table 2. Properties of the tungsten carbide material (M.A.Ford 1998; MEMSnet 2009)

Density	14500 kg m^{-3}
Knoop Hardness (KH)	1870
Vickeres Hardness (VH)	1730

3.2.2 316L STAINLESS STEEL

The machining of the carbide end mill tool was performed on a 316L stainless steel workpiece material. Stainless steel 316L is the low carbon content version of 316 Stainless Steel. It is an austenitic stainless steel with iron, chromium, nickel, molybdenum and manganese. The chemical composition of 316L stainless steel and its mechanical properties are described in Table 3 and Table 4 respectively.

Table 3. Composition of stainless steel 316L alloy (ASTM A 240, 2007)

ELEMENT	PERCENTAGE (%)
Iron(Fe)	68.2
Chromium (Cr)	17.2
Nickel (Ni)	10.9
Molybdenum (Mo)	2.1
Manganese (Mn)	1.6

Table 4. Mechanical properties of stainless steel 316L (Azom 2009)

Grade	Tensile Strength (MPa)	Yield Strength 0.2% Proof (MPa)	Elongation (% in 50 mm)	Hardness	
				Brinell (HB)	Rockwell B (HR B)
316L	485	170	40	95	217

3.2.3 HAAS OFFICE MILLING MACHINE (OM2)

HAAS OM2 CNC termed as Office Mill 2(OM2) micromilling system was used to perform micromachining. The tool runout measurements of the spindle for different cutting conditions were measured on the HAAS micromilling system. The main feature of the HAAS OM2 were that it can achieve a positioning accuracy of ±5 µm (±0.0002”) and repeatability of ±3 µm (±0.0001”) [1]. The system is highly stable for even high spindle speeds and the machine’s high positional accuracy make it an ideal choice for any micromachining process. The OM2 micromachining system was capable to run upto 50,000 rpm. The workpiece was mounted on a trunnion and tool was mounted on to the spindle using a collet. Required NC programs were developed on FeatureCAM CAD software.

3.2.4 HAAS VF1

The Haas VF-1 is a vertical milling center was used to run the tool failure tests for micromilling. The CNC machining system was used for different extreme cutting conditions to analyze the tool failure in micromilling process. The high thrust capacity of the system upto 11,000N makes the system highly reliable for crash tests. The HAAS VF1 system can be used to achieve a positioning accuracy of ±5 µm (±0.0002”) and repeatability of ±3 µm (±0.0001”) [1]. The system is capable of running at different cutting conditions and has a maximum spindle speed of 7,000 rpm. Flood coolant Rustlick WS-500 A halogen free heavy duty soluble oil was used during the crash tests for tool failure.

---

[1] http://www.haasautomation.com.

3.2.5 KEYENCE LK-G157 LASER

Precise positioning of the tool and dynamic measurements of the tool deflection play an important role for any micromachining process. A high displacement sensitive device is required when working at the microlevel of machining. Keyence LK-G157 laser system was used to measure the spindle runout for different speeds and cutting conditions. This laser system is a 2-D displacement measuring device used to the position the tool with respect to the workpiece and to measure the deflections of the spindle for during machining process with an accuracy of ±0.5% and resolution of 0.5μm [2].

The measurement sensor was used to position the electrode in close proximity to the workpiece which is in the order of a few microns and to measure the distance traversed by the electrode. The provided software LK-Navigator enables the user to optimize the laser beam to effectively measure the surface being measured.

3.2.6 UNIST MIST COOLUBRICATOR SYSTEM

UNIST Coolubricator systems are self-contained, positive displacement continuous spray systems. It is designed primarily for the application of new generation high efficiency lubricants. The system operates when the adjustable pulse generator cycles the metering pump. The output and the metering pump stroke are also adjustable.

---

[2] http://www.keyence.com.

Liquid output is adjusted with the brass knob on each metering pump. The lubricant spray is delivered through an external mix nozzle coupled to a 5' co-axial hose. The magnetic base at the hose/nozzle connection allows for easy relocation of the nozzle. Coolube 2210EP coolant is used for the mist spray. 2210EP is an environmentally acceptable vegetable based lubricant for use with the UNIST mist systems [3].

3.3 TOOL/ WORKPIECE POSITIONING

The relative position of the tool with work piece is highly important in the micromachining process. Any misalignment of the tool with workpiece would lead to unexpected machining process and may affect the tool life drastically. Considering the scale at which the machining is done the positioning of the tool with respect to cutting tool is highly important in micromachining process. High technology positioning probes are used in the industry for the precise positioning of the workpiece which operate by contact methods. Such methods though are effective but would involve high equipment costs. The positioning of the tool for the current experiments was done by use of displacement laser sensors to measure the relative position of the tool with the workpiece. Several experiments were conducted to study the consistency and accuracy of using lasers for the positioning of the tool with workpiece.

---

[3] http://www.unist.com.

The positioning is done by focusing the laser from Keyence laser setup ‘2’ on the shank of the cutting tool ‘1’ first and then focusing the laser on the face of work piece ‘3’ to measure the distance between them. The positioning setup and laser focusing can be shown in Figures 11 and 12 respectively. The tool is then positioned by offsetting it by the required distance. This approach was used for both the X- and Y- axes. This method gave consistent results and was very accurate in positioning the tool. The tool position with respect to Z- axis is highly important as any error in positioning would result in either less or more depth of cut than desired. Any small increase in depth of cut is of a significant amount for a microtool and would result in the tool failure due to increase in chip load along Z-axis. Any undercut than required would result in loss of required machining geometry. So the tool positioning for Z- axis has to be properly measured. The conventional contact method of using a thin sheet of paper for zeroing the tool with respect to Z-axis would break the tool for any additional depth more than the workpiece surface. Hence a non-contact laser method is used for positioning the tool with Z-axis. The laser beam is focused on a cantilever beam made of rubber that would deflect for any contact of the tool. The deflection is then detected using the laser; this deflection would help to detect the position of the tool and hence helps to position the tool with respect to the surface of the work piece. Several set of experiments were conducted and the laser method has shown repeatability upto 1.5 μm.

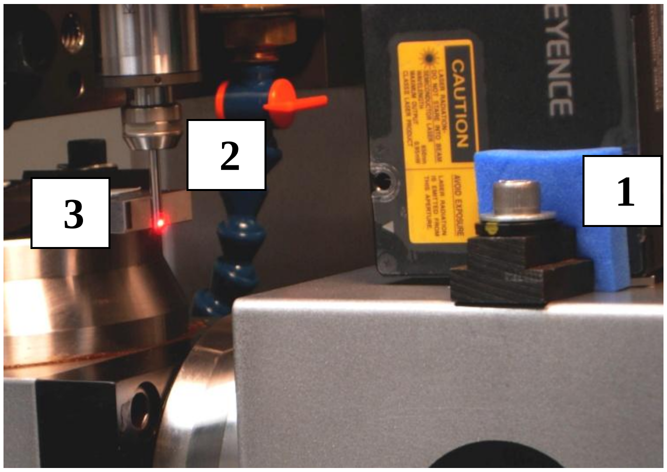

Figure 11. Setup showing the Keyence laser and cutting tool for tool positioning
1: Keyence laser, 2: Cutting tool and 3: Workpiece

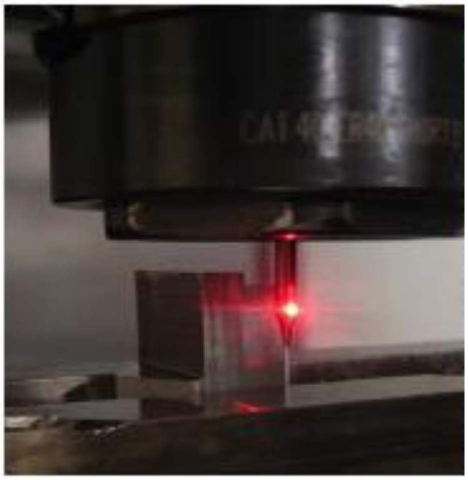

Figure 12. Non contact Keyence laser used for tool positioning

3.4 EXPERIMENTS

3.4.1 THREE POINT BENDING TEST OF CUTTING TOOL

The mechanical properties of the tungsten carbide tool are very important for testing and analysis to be performed. A three point flexure test was performed for the tungsten carbide end mill. The flexural test measures behavior of the tool when subjected to simple beam loading. Maximum fiber stress and maximum strain are calculated for increments of load. Flexural strength is defined as the maximum stress in the outermost fiber. In this test, the area of uniform stress is quite small and is concentrated on the centre loading point. The flexure test of microtool can be compared to a circular beam, on which a simple concentrated force is exercised in the centre of the beam with a load of P. The experiment was performed Instron model 4411 universal testing machine. The strain rate of the test was maintained at 101.6 mm/min (4 in/min) and the test was done till the failure of the tool. Tool properties were derived from the plot obtained from the load applied on the microend mill and the corresponding deflection data.

3.4.2 TOOL RUNOUT AND DEFLECTION MEASUREMENT

Radial runout, or eccentricity, of the cutter is a common problem in multiple cutting edge, interrupted machining operations. Well-known effects include premature cutting edge failure due to periodic variations in the chip load and force, as well as increased machined surface roughness (Tony et al. 2007). The current research is focused on the measuring tool runout and tool deflection while cutting and thereby predict the failure of the cutting tool under extreme conditions of the tool deflection during machining using finite element techniques. Figure 13 shows the micromachining setup used for tool runout measurement. Highly sensitive Keyence LK-G157 displacement laser system '1' was used to measure the dynamic data of tool eccentricity during machining operations. Several experiments were conducted to measure the tool runout for different spindle speeds. The tool deflection under different cutting conditions was also measured to study the effect of deflection on cutting tool. The important aspect of these experiments was to collect the dynamic deflection data while machining.

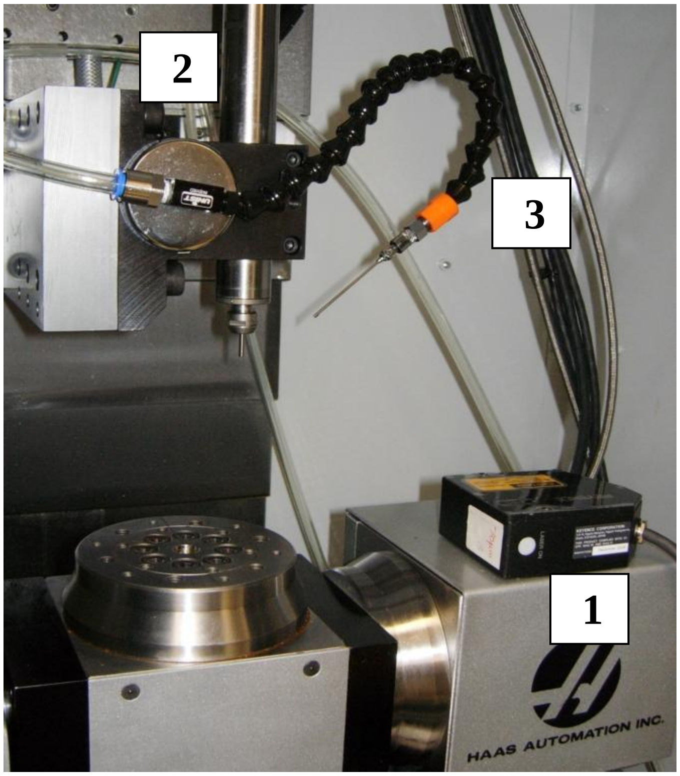

Figure 13. HAAS OM2 micromachining system used for runout measurement
1: Keyence laser, 2: Spindle of OM2 and 3: Mist coolant hose

The experiments were performed on a block of 316L stainless steel. End milling was performed on the HAAS OM2 micromachining system using MA Ford’s carbide end mill tools (Ø1.016 mm, 2 flute) in mist coolant. The tool was machined for a straight line cut with a constant axial and radial depth of cut. All tools were ultrasonically cleaned in alcohol before any machining and measurement. The mist coolant was applied at 135° relative to the feed direction and at a distance range of 25-30 mm from the tool through the coolant hose ‘3’ of Unist mist system. Coolube 2210EP coolant was used for the mist spray. The programming for the CNC machining was performed using FeatureCAM software. Tables 5 and 6 show the parameters used for tool runout and deflection measurement.

Table 5. Process parameters for measuring tool runout

Microcutting tool	Gauge pin, Ø3.175mm
Work piece material	316L Stainless steel
Spindle speed	0 rpm (Stationary),6,000 rpm and 10,000 rpm

Table 6. Process parameters for measuring tool deflection when machining

Microcutting tool	Ø1.016 mm, 2 flute
Work piece material	316L Stainless steel
Feed per tooth /Chip load	10 µm/tooth
Axial depth of cut	0.35 mm.
Radial depth of cut	0.56 mm
Spindle speed	15,000 rpm and 25,000 rpm
Coolant	Unist mist spray

3.4.3 CRASH TEST FOR TOOL FAILURE

Failure of the microend mills was studied for different cutting conditions by studying the maximum cutting force that could result in tool failure. Several experiments were performed to see the behavior of tools under extreme conditions so that the tool failure can be predicted. End milling was performed on the HAAS VF1 machining system using MA Ford's carbide end mill tools (Ø1.016 mm, 2 flute) on 316L stainless steel workpiece material. The tool was run at different cutting conditions with gradual increase in width of cut along the feed direction where the tool would cut the width equal to its diameter as it reaches the length of the workpiece. Figure 14 clearly shows the tool path and the solid model of the representing the crash test experiment. This experimental setup would help to analyze the shear area of cut where the tool fails which can be further used to study the cutting force acting on the tool.

Table 7. Process parameters for crash tests

Microcutting tool	Tungsten carbide, Ø1.016 mm, 2 flute
Work piece material	316L Stainless steel
Feed per tooth /Chip load	38 µm/tooth, 76 µm/tooth, 114 µm/tooth and 152 µm/tooth
Axial depth of cut	0.35 mm and 0.70 mm
Radial depth of cut	Gradually increasing from 0 to 1.016 mm
Spindle speed	6,000 rpm
Coolant	Flood coolant - Rustlick WS-500 A

Table 7 shows different process parameters used for the crash tests. The first part of the experiment was to set up the work piece and align the tool in the X axis, Y axis and Z axis. Tool - work piece positioning was done as described in section 3.3 using the Keyence LK-G82 laser system. Different cutting conditions were employed to study the failure of the tool. During machining the microtool fails at a certain width of cut where the cutting force exerted on it would cause high stress and result in tool failure. The distance where the tool fails is measured from the experiment and then used to calculate the shearing force acting on the tool and thereby calculating the feed component of the cutting force acting on the cutting tool. This result is further compared with the results obtained from the finite element methods and the effect of cutting force on the microtool was analyzed.

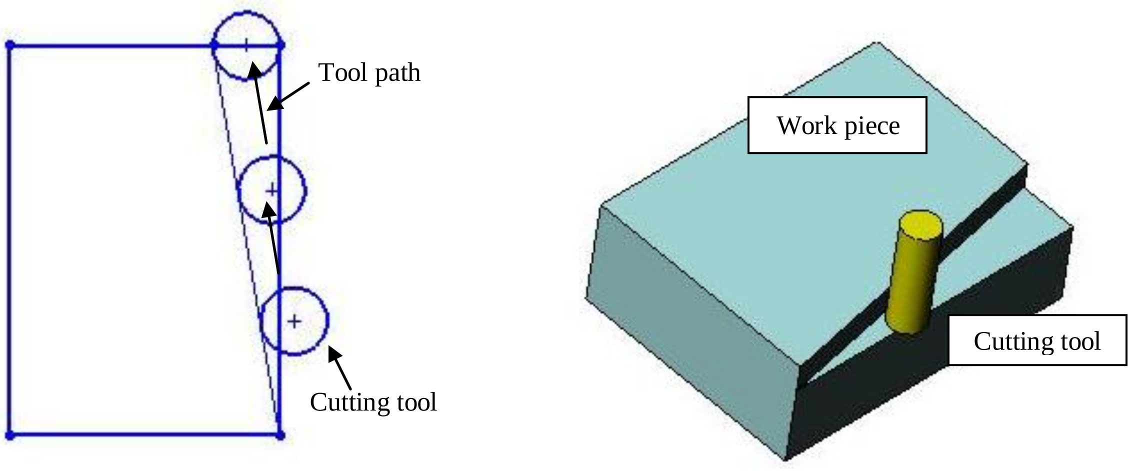

(a) (b)

Figure 14. Cutting tool path
(a) 2 D sketch of the tool path showing the increase area of cut
(b) Solid model showing the tool path for crash tests

4. MODELING OF CUTTING FORCE AND TOOL FAILURE

Modeling of cutting forces is important to predict the cutting forces acting on the microtool during machining. A mathematical model was developed to estimate the cutting force in feed direction that would fail the tool by measuring the shear area of cut at the point of tool failure. The friction area of the tool was also modeled considering the tool runout in the directions along and perpendicular to feed. As the cutting force is proportional to area of cut, the friction area calculated helps to understand its effect on the cutting tool. Figure 15 shows the position of cutting tool, line of cut and different areas of cut modeled for the crash test performed.

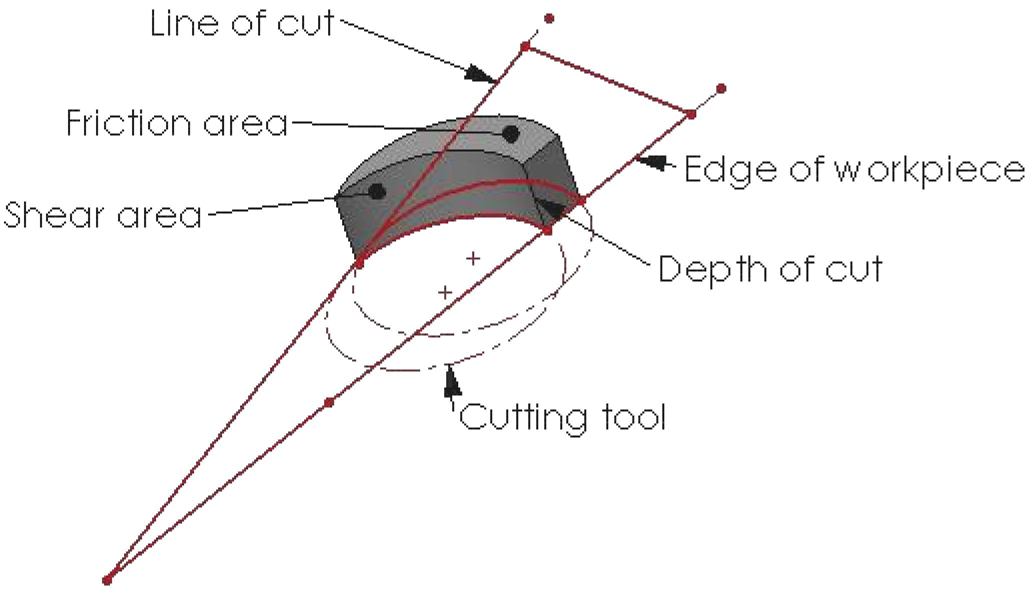

Figure 15. Shear and friction area of cut for two consecutive positions of the cutting tool

4.1 MODELING OF CUTTING FORCE USING SHEAR AREA

The cutting force in feed direction was modeled to predict the cutting force that would result in tool failure. Shear force on the tool was first measured by calculating the shear area due to cut and then the cutting force was calculated from the Merchant's equation. The shear area due to cut was modeled by mathematically calculating the area of cut at the point where the tool fails. Figure 15 shows the shear area measured. The cutting tool, line of cut, chip load etc., were represented by geometric entities and the shear area was modeled.

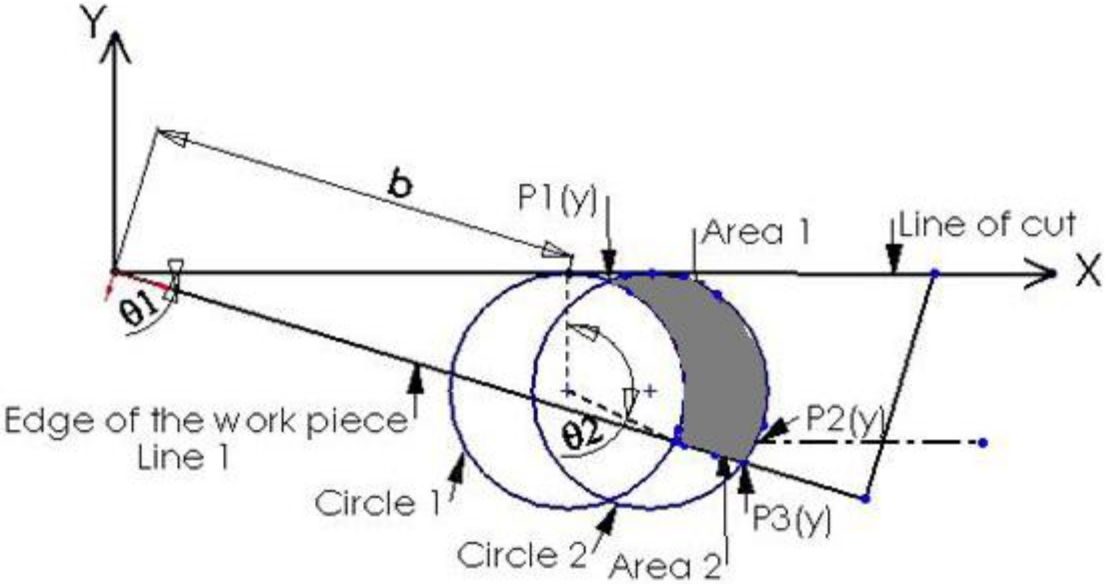

Figure 16. Geometric representation of cutting tool, work piece and line of cut

The X-axis in the Figure 16 represents the line of cut of the cutting tool. The two circles, circle 1 and circle 2, in Figure 16 represent the cutting tool positions separated by distance equal to chip load (f_c). The edge of the 316L workpiece was represented by line 1. These geometric entities were used to model the shear area in Figure 15. The included angle 'θ_2' is measured using the points of intersection P_1, P_2 and P_3. P_1 is the point of intersection of circle 1 and 2 and P_2 and P_3 are the points of intersection of line 1 with circles 1 and 2 respectively. The distance 'b' was measured from the crash tests where the microtool fails. From above geometric considerations the shear area of cut is equal to the arc length of the circle 1 between the two lines, line 1 and X-axis, multiplied by the height equal to axial depth of cut (h) of the tool. The shear force (F_s) is hence obtained by multiplying the shear area with the shear strength of the workpiece material 316L SS.

Hence the shear force acting on the tool is derived in Appendix (B1) as,

$$F_s = \tau * R * \theta_2 * h * \left(\frac{\pi}{180}\right) \tag{1}$$

Based on the shear force measurement, the cutting force F_c acting along the direction of feed defined from Merchant equations (Groover 2004) as,

$$F_c = F_s * \left(\frac{\cos(\beta\text{-}\alpha)}{\cos(\phi+\beta\text{-}\alpha)} \right) \tag{2}$$

where

α = end rake angle

β = friction angle

ϕ = shear plane angle

Therefore from equations (1) and (2) the equation for shear force is defined as

$$F_c = \tau * R * \theta_2 * h * \left(\frac{\pi}{180}\right) * \left(\frac{\cos(\beta-\alpha)}{\cos(\phi+\beta-\alpha)}\right) \tag{3}$$

The above equation (3) defines the cutting force acting on the tool in the feed direction. The end rake angle α is estimated from the geometry of the cutting tool. The friction angle β is obtained from the coefficient of friction values between the tungsten carbide cutting tool and 316L stainless steel work piece.

For a given coefficient of friction (μ), friction angle (β) is defined as,

$$\beta = \tan^{-1}(\mu) \tag{4}$$

The shear plane angle (ϕ) is estimated from the friction angle and the tool rake angle by the Merchant equation (Groover 2004) as,

$$\phi = 45 + \frac{\alpha-\beta}{2} \tag{5}$$

The above set of equations (1) through (5) were used to estimate the cutting force acting on the tool, at the tool failure, in the direction of feed using the principle of shear area of cut during machining.

4.1.1 EFFECT OF CUTTER RUNOUT IN FEED DIRECTION ON CUTTING FORCE

The effect of cutter runout on cutting force acting on the tool was studied to understand the significance of cutter runout on the cutting tool. Runout '*e*' was considered in the direction of feed. The new shear area was calculated considering the runout position and the new cutting force was calculated considering the tool runout.

Hence the cutting force acting on the tool considering the tool runout was derived in Appendix (B1) as,

$$F_{ce} = \tau * R * \theta_{2e} * h * \left(\frac{\pi}{180}\right) * \left(\frac{\cos(\beta-\alpha)}{\cos(\phi+\beta-\alpha)}\right) \qquad (6)$$

where θ_{2e} is the included angle considering the runout '*e*' in the direction of feed.

4.2 MODELING OF FRICTION AREA AND EFFECT OF CUTTER RUNOUT

The measure of friction force acting on the cutting tool is highly important to study the behavior of the microcutting tool. As the friction force is proportional to friction area (A_f), the increase in friction area due to cutter runout in different directions helps to understand the effect due to cutter runout. Increase in friction area due to runout increases the cutting energy by the tool to cut the additional area. A mathematical model was developed to estimate the friction area of cut from the geometric assumptions made in section 4.1. The method was further extended to measure the additional increase in friction area due to cutter runout (e) in the directions along and perpendicular to the feed.

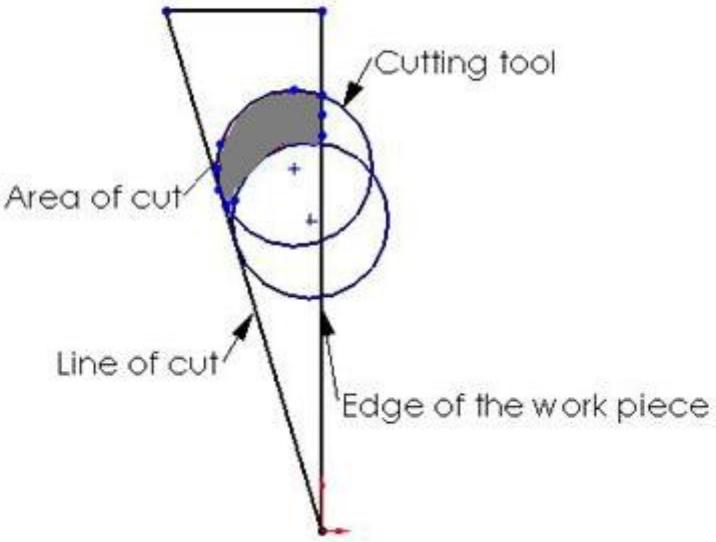

Figure 17. Simplified sketch describing friction area (A_f) of cut and geometric representation of cutting tool, work piece and line of cut

Figure 17 explains the friction area involved for the two tool positions separated by distance equal to chipload (f_c). The geometric representations of cutting tool positions, workpiece and line of cut, from section 4.1 and Figure 16 were used to model the friction area.

From Figure 16, Friction Area (A_f) = Area 1 + Area 2 (7)

Solving equation (6), the friction area (A_f), derived in Appendix (B3), is defined as,

$$A_f = f_c * \left(-R + \sqrt{R^2 - \frac{f_c^2}{4}} + \left(\left(b * \sec\theta_1 + f_c \right) * \cot\theta_1 + R - k_2 \right) * \sin^2\theta_1 \right) +$$

$$(b * \sec\theta_1) * (f_c * \cot\theta_1 + k_1 - k_2) * \sin^2\theta_1 + \frac{R^2}{2}(\gamma - \frac{\sin 2\gamma}{2})\Big]_{\gamma_3}^{\gamma_2} + \frac{\cot\theta_1}{2} * \left((P_2(y)^2) - (P_3(y)^2) \right) \quad (8)$$

where $P_1(y)$, $P_2(y)$, $P_3(y)$, can be obtained from geometric entities in section 4.1. Hence the equation (7) was used to estimate A_f, the friction area of cut geometrically from basic assumptions and experimental data.

4.2.1 FRICTION AREA WHEN RUNOUT IS IN THE DIRECTION OF FEED

The effect of cutter runout is an important factor for microtool. The cutter runout during machining increases friction area which is proportional to the friction force acting on the tool. The cutter runout in the directions along and perpendicular to feed direction were considered for the mathematical modeling. The method used to measure friction area from section 4.2 was extended to estimate the friction area (A_{r1}) when runout is in the direction of feed.

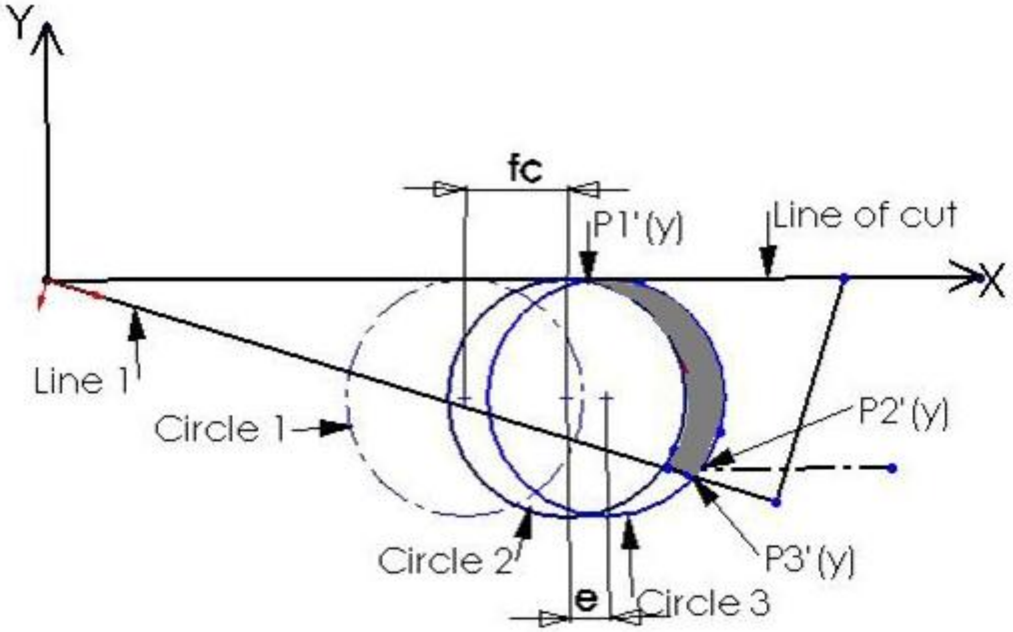

Figure 18. Geometric representation of friction area when runout is in direction of feed

Figure 18 describes the geometric entities considering the effect of cutter runout ‘e’ in the feed direction and the corresponding shaded additional friction area (Ar1) enclosed between the circles 2 and 3. Following the approach used in section 4.2 for the equation (7) the area $A_{r1,}$ derived in Appendix (B4), was obtained as,

$$A_{r1}= e * \left(-R+\sqrt{R^2-\frac{e^2}{4}}+\left(\left(b*\sec\theta_1+f_c+e\right)*\cot\theta_1+R-k_2'\right)*\sin^2\theta_1\right)+$$

$$\left(b*\sec\theta_1+f_c\right)*\left(e*\cot\theta_1+k_1'-k_2'\right)*\sin^2\theta_1+\frac{R^2}{2}\left(\gamma'-\frac{\sin 2\gamma'}{2}\right)_{\gamma_3'}^{\gamma_2'}+\frac{\cot\theta_1}{2}*\left(P_2'(y)^2-P_3'(y)^2\right) \quad (9)$$

where P_1' is the point of intersection of circle 1 and 2 and P_2' and P_3' are the points of intersection of line 1 with circles 1 and 2 respectively.

Equation (9) was used to find $A_{r1,}$ the additional friction area of cut due to cutter runout in the direction of cut, from basic geometric assumptions and experimental data. Therefore the total friction area when the runout is in direction of feed is given by sum of equations (7) and (9).

4.2.2 FRICTION AREA WHEN RUNOUT IS PERPENDICULAR TO THE DIRECTION OF FEED

The additional friction area (Ar_2) for runout perpendicular to the direction of feed was modeled using geometric assumptions for cutting tool positions and runout described is section 4.2. Figure 19 describes the condition when the cutter runout (*e*) is perpendicular to the direction of feed. For a runout equal to '*e*' the position of tool can be defined using the circle 4. The shaded area enclosed between circles 2 and 4 is the additional area due to cutter runout.

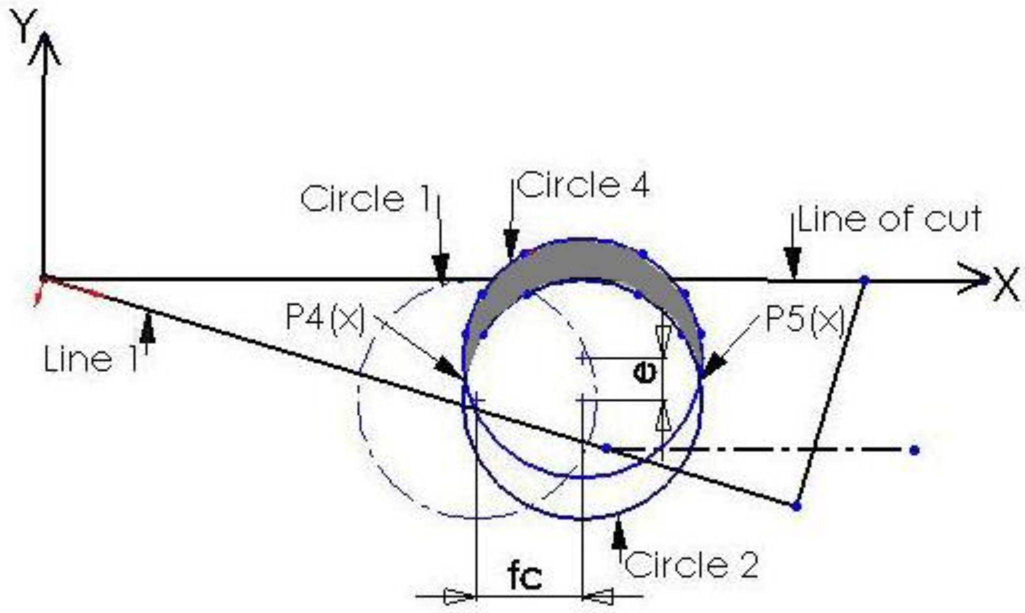

Figure 19. Geometric representation of friction area when runout is perpendicular to the direction of feed

Hence from the geometric assumptions the additional area due to runout in the direction perpendicular to feed (A_{r2}) was modeled as,

$$A_{r2} = 2*e*\sqrt{R^2-\frac{e^2}{4}} \tag{10}$$

Equation (10) was used to find $A_{r2,}$ the additional friction area of cut due to cutter runout perpendicular to feed direction, from basic geometric assumptions and experimental data. Therefore the total friction area when the runout is perpendicular to feed is given by sum of equations (7) and (10).

From equations (9) and (10), we can observe that friction area due to runout perpendicular to feed (A_{r2}) is independent of chipload unlike friction area for runout in direction of feed (Ar1) which is a factor of chip load (f_c), width of cut, line of cut etc. The equations modeled in section 4.2 hence are useful to estimate the friction area during cutting and the effect of cutter runout on friction area. Complete derivation of the above equations is presented in Appendix B. The modeled equations (8), (9) and (10) were used to calculate the friction area and area due to runout where the tool fails. These estimates help to understand the effect of cutter runout direction on microcutting tool.

4.3 ESTIMATION OF SPECIFIC ENERGY FROM CUTTING FORCE

Estimation of specific energy (*u*) for 316L was done from cutting force calculated from crash tests. Specific energy tends to remain approximately constant for a given work material operating under different cutting conditions (Shaw, 2005). The specific cutting energy will be independent of cutting speed provided a large built-up edge is not obtained. However, the specific energy is affected by the workpiece chemistry and structure, the rake angle of the tool and the undeformed chip thickness or feed per revolution. Specific energy (u) is related to undeformed chip thickness (*t*) as

$$u \sim 1/t^{0.2} \qquad (11)$$

The principle cutting force responsible for the power consumed (F_p) is estimated as

$$F_p = u * t * h \qquad (12)$$

The cutting force component in the feed direction is approximated to be equal to one half of F_p.

Therefore,

$$F_c = 1/2 * u * t * h \qquad (13)$$

where

u = Specific energy

F_p = Cutting force responsible for power

F_c = Cutting force in the direction of feed

h = Depth of cut

t = Undeformed chip thickness

Table 8. Approximate values of specific energy for different materials cut with α = 0° and t= 0.010in (0.25 mm) (Shaw 2005)

Material	u_0 (10^8 J m^{-3})
Aluminum alloy	7.02
Gray cast iron	10.53
Free- machining brass	10.53
Free-machining steel (AISI 1213)	17.55
Mild steel (AISI 1018)	21.06
Titanium alloys	35.10
Stainless steel(18-8)	49.14
High-temperature alloys (Ni or Co base materials)	49.14

Table 8 describes the approximate specific energy values of different materials. Following the above set of equations (11) through (13) were used to estimate the specific energy (*u*) from the cutting force calculated from the crash tests.

4.4 EQUATIONS FOR FLEXURE TEST

Calculation of Young's modulus and maximum flexure stress are two important results that are obtained from flexure test done using a three point bending on the microtool.

The plot of load vs. deflection curve obtained from the flexure test is used for obtaining the required values.

The flexure stress for a circular beam can be calculated using the equation (Gere et al. 1972),

$$\sigma_f = \frac{P * L}{\pi * r^3} \tag{14}$$

And flexure strain is measured using the equation,

$$\epsilon_f = 6 * D * \frac{2 * r}{L^2} \tag{15}$$

The modulus of elasticity in bending (E) for the tool is obtained from the stress strain plot obtained with the above data. The modulus is the gradient of the stress-strain graph for the region that obeys Hooke's law.

where,

σ_f = Stress in outer fibers at midpoint, (MPa)

ϵ_f = Strain in the outer surface, (%)

D = Maximum deflection of the center of the beam, (mm)

E = Modulus of elasticity in bending, (MPa)

I = Section inertia moment of wire, for circular cross section, (mm^4)

L = Support span, (mm)

P = Load at a given point on the load deflection curve, (N)

r = Radius of shank of cutting tool, (mm)

5. RESULTS AND DISCUSSION

5.1 THREE POINT BENDING TEST RESULTS

The results from the three point bend test were used to estimate the mechanical properties of the tungsten carbide microtool. Flexure stress and flexure strain were calculated from the experiment were used to estimate the Young's modulus of the cutting tool. The equations (41) through (43) were used to plot the stress vs strain graph of the flexure test and to estimate the material properties of the tool.

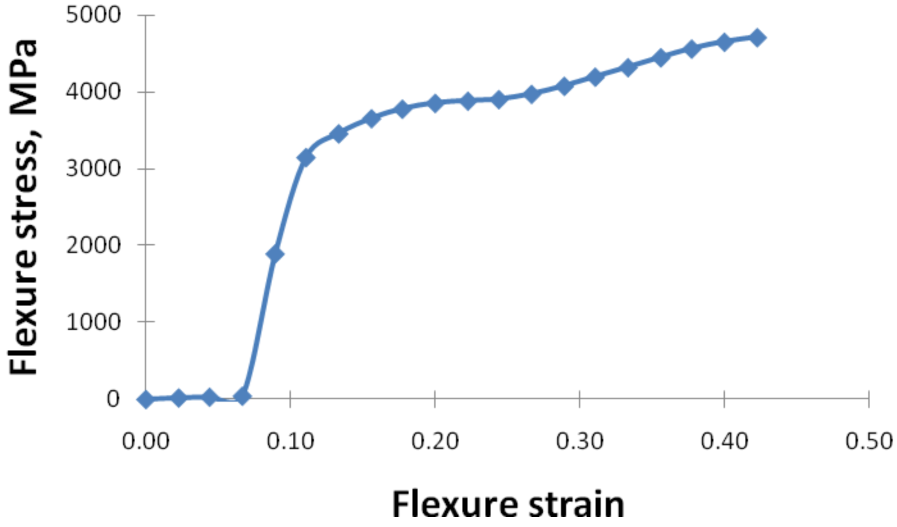

Figure 20. Stress - strain plot obtained from flexure test of tool

Table 9. Flexural stress, strain values from three- point bend test

No.	Flexure Stress, σ_f, MPa	Flexure Strain, ϵ_f
1	0.00	0.00
2	19.92	0.02
3	30.25	0.04
4	43.11	0.07
5	1896.62	0.09
6	3153.62	0.11
7	3463.31	0.13
8	3660.33	0.16
9	3783.80	0.18
10	3860.05	0.20
11	3889.06	0.22
12	3908.62	0.24
13	3977.45	0.27
14	4082.70	0.29
15	4202.13	0.31
16	4325.60	0.33
17	4453.79	0.36
18	4567.82	0.38
19	4656.88	0.40
20	4716.93	0.42

Table 9 shows the flexure stress and strain obtained from equations (41) and (43) described in section 4.4 for the flexure test. The slope of the curve in Figure 20 obeying the Hooke's law was considered for the Young's modulus of the tool. Table 10 shows the results obtained from 3-point bend test. The brittle nature of tool explains the premature failure of the cutting tool under high cutting forces. As the tool was brittle the maximum values of bending stress and Young's modulus from the experiment were considered for flexure strength and Young's modulus respectively in the FEA of tool.

Table 10. Properties of tungsten carbide microtool obtained from 3-point bend test

Flexure strength	4,700 MPa
Young's Modulus	92.7 GPa

5.2 TOOL RUNOUT MEASUREMENT RESULTS

Several experiments to measure the tool runout and tool deflection while cutting were performed as discussed in section (3.4.2). Tool deflection was measured for several conditions for different spindle speeds when the tool was machining as well as not machining. Effect of mist spray on tool deflection was also noted.

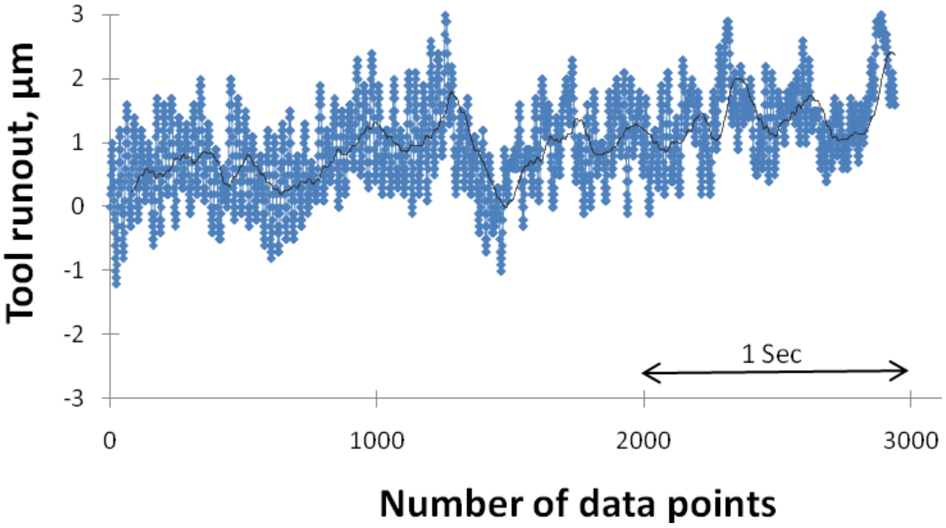

Figure 21. Tool runout when the machine is stationary. (Endmill-Ø1.016 mm x 2 flute, N= 0 rpm, f_c=0). The trendline in the figure represents the average profile of 'drifting' of the electronic system

Figure 21 shows the maximum deflection in the tool, when the spindle was stationary, was approximately equal to 2 µm on HAAS OM2. The trendline in Figure 21 follows a function of random pattern within ±1 µm. This deflection of tool accounts for the 'drifting' of the electronic system.

For a spindle speed of 6,000 rpm Figure 22 shows a maximum tool runout of 3 µm. A ±1 µm 'drifting' of electronic system can be observed from the figure. Hence the system has a negligible tool runout of 1 µm at 6,000 rpm spindle speed.

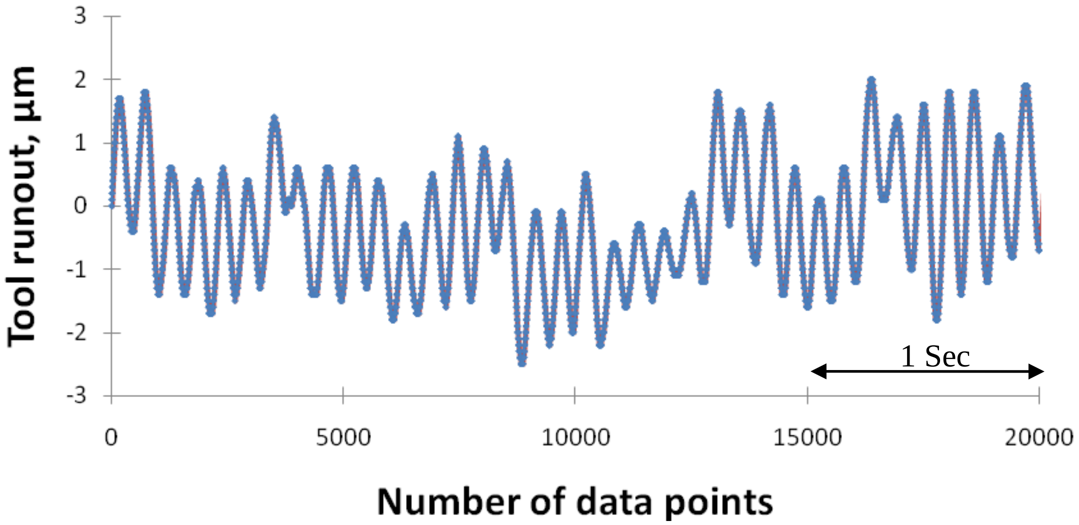

Figure 22. Tool runout for a spindle speed of 6,000 rpm (Endmill-Ø1.016 mm x 2 flute)

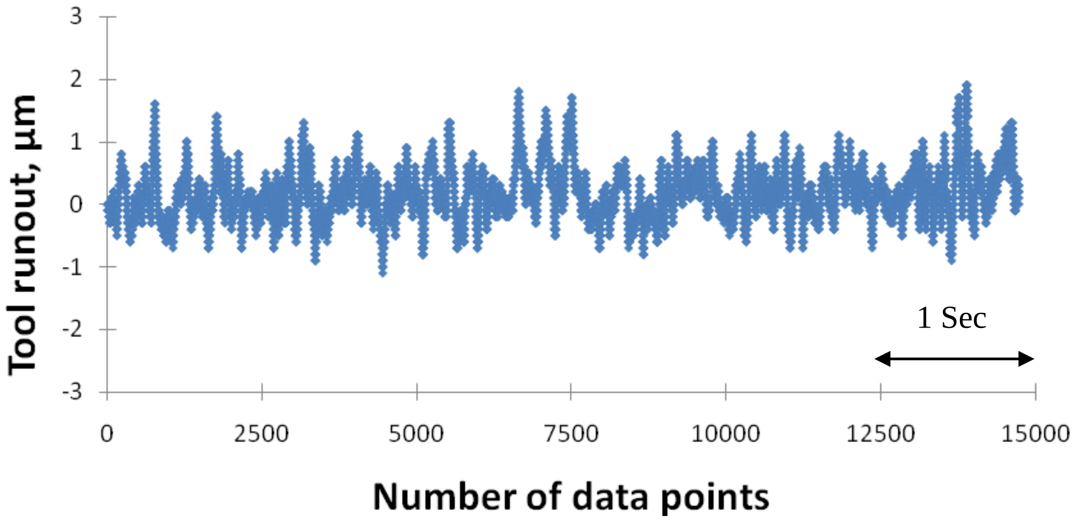

Figure 23. Tool runout for a spindle speed of 10,000 rpm (Endmill-Ø1.016 mm x 2 flute)

Figure 23 shows the tool runout at 10,000 rpm equal to 2 µm which includes the effect of the electronic system 'drifting' of ±1 µm. Hence the system has a negligible tool runout at 10,000 rpm spindle speed.

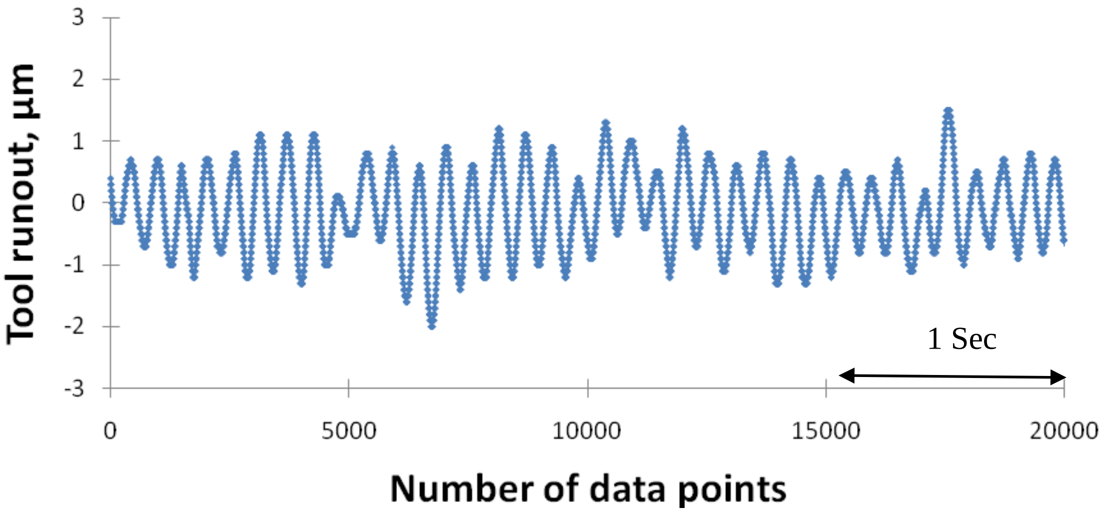

Figure 24. Tool runout for stationary spindle with mist coolant (Endmill-Ø1.016 mm x 2 flute). Mist spray angle 135° relative to the feed direction, 25-30 mm from microtool

Figure 24 shows that the deflection in a stationary spindle due to mist spray was approximately equal to 2 µm with a +1 µm of electronic system ‘drifting’. The plot shows that the effect of mist spray on tool runout is highly negligible.

Tool runout for spindle speeds 6,000 rpm and 10,000 rpm after removing the effect of ‘drifting’ was calculated using the Figures 21, 22 and 23. The tool runout values when the machine was stationary in Figure 21 correspond to the ‘drifting’ of electronic system and to remove the effect of phase in the electronic system the values were sorted from lower to higher values and an average trend was observed. The final tool runout was obtained by subtracting the average values of spindle speeds 6,000 and 10,000 rpm from corresponding values in 0 rpm. From Figure 25 it was observed that the final runout neglecting the effect of ‘drifting’ to be less than 1 µm.

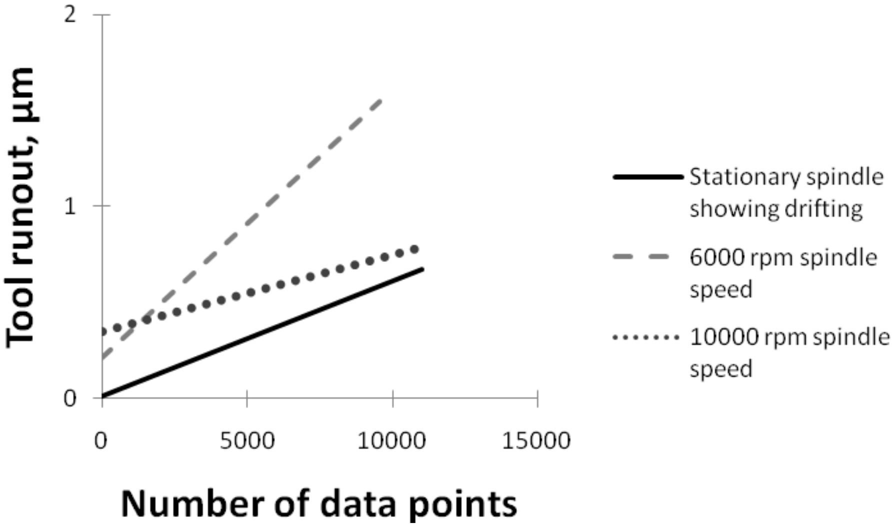

Figure 25. Final runout after eliminating ‘drifting’ for a spindle speed of 6,000 rpm and 10,000 rpm (Endmill-Ø1.016 mm x 2 flute)

The low values of runout data obtained for different spindle speeds shows the integrity of the HAAS OM2 micromachining system. The above runout data obtained for different conditions is highly important for micromachining. Tool runout was in many cases assumed constant or predicted from variations in cutting forces. Bao et al. (2000b) estimated the tool runout by inspecting the difference of peaks of cutting force data measured. This method though would help us to find the cutter runout is not highly preferred because of the complexity involved in measuring the cutting force and then comparing them to get the runout data. The use of displacement laser to measure the tool runout is highly easy and gives the data directly instead of estimating it. The current method can be used to collect runout data continuously throughout the machining process at any machining condition.

5.2.1 TOOL DEFLECTION WHEN MACHINING

Tool deflection was measured when machining to understand the effect of tool deflection during machining and extend it to tool behavior.

Figure 26 shows the tool deflection data when machining a 316L stainless steel workpiece using a 2 flute microend-mill of 1.016 mm cutter diameter for spindle speed of 15,000 rpm. The maximum tool deflection was observed to be equal to ± 8 μm at two positions of the machining process. These two points correspond to the start and end of machining. The drifting of electronic system was observed to be equal to ± 2 μm.

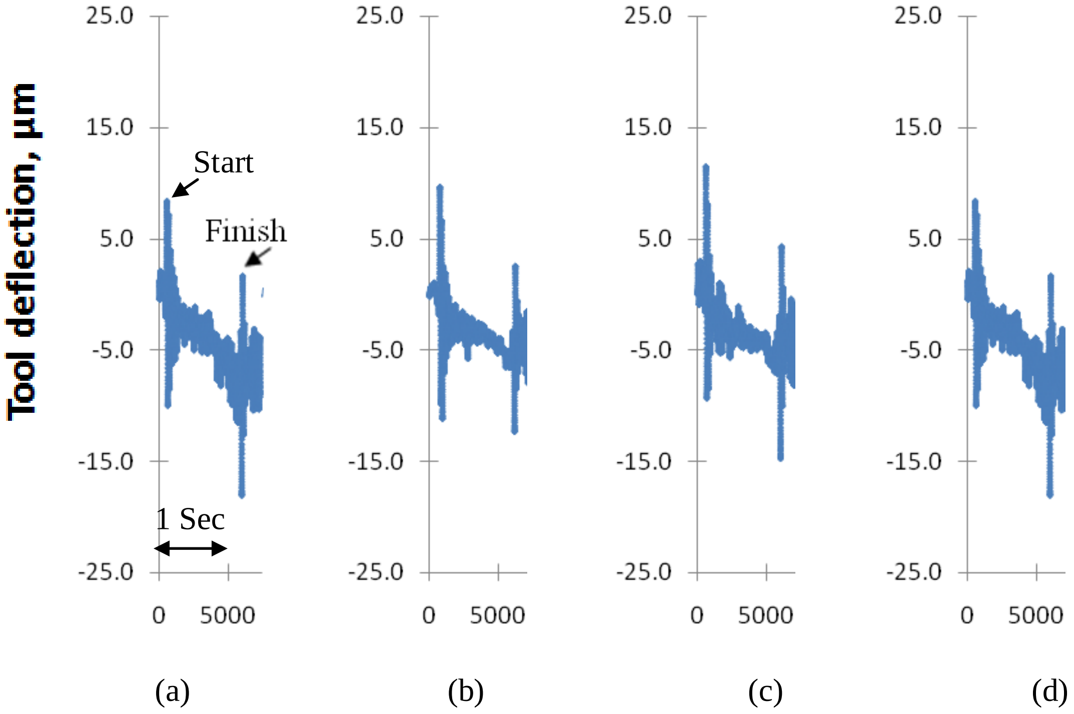

Figure 26. Tool deflection when machining 316L SS workpiece (Endmill-Ø1.016 mm x 2 flute, N=15,000 rpm, f_c=10 µm/tooth, depth of cut =0.35 mm, width of cut=0.56 mm, mist coolant). Repeatability is illustrated parts (a) – (d).

Figure 27 shows the tool deflection data when machining a 316L stainless steel workpiece using a 2 flute microend-mill of 1.016 mm cutter diameter for spindle speed of 25,000 rpm. The maximum tool deflection was observed to be equal to ± 20 µm at two positions of the machining process. These two points correspond to the start and end of machining. The deflection of tool was observed to increase with increase in spindle speed. The drifting of electronic system was observed to be equal to ± 2 µm.

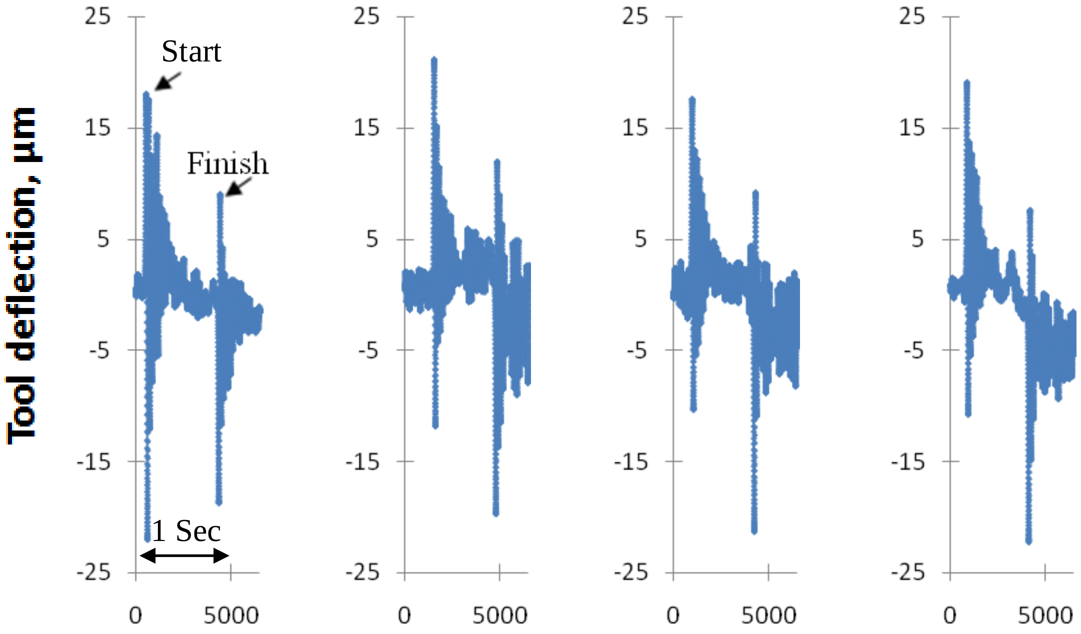

(a) (b) (c) (d)

Figure 27. Tool deflection when machining 316L SS workpiece (Endmill-Ø1.016 mm x 2 flute, N=25,000 rpm, f_c=10 µm/tooth, depth of cut =0.35 mm, width of cut=0.56 mm, mist coolant). Repeatability is illustrated in parts (a) – (d).

The current method measures tool runout directly and gives a clear perspective of tool deflection during machining unlike other methods where cutter runout was estimated from cutting force data.

5.3 CRASH TEST RESULTS

Cutting force in the feed direction was measured using the equation (3) in section 4.2 from the crash tests using microtool. Figure 28 shows the 316L SS workpiece after the crash test. The position where tool failed was clearly observed from the work piece and the corresponding distance where the tool failed (b) was measured for each of the crash tests.

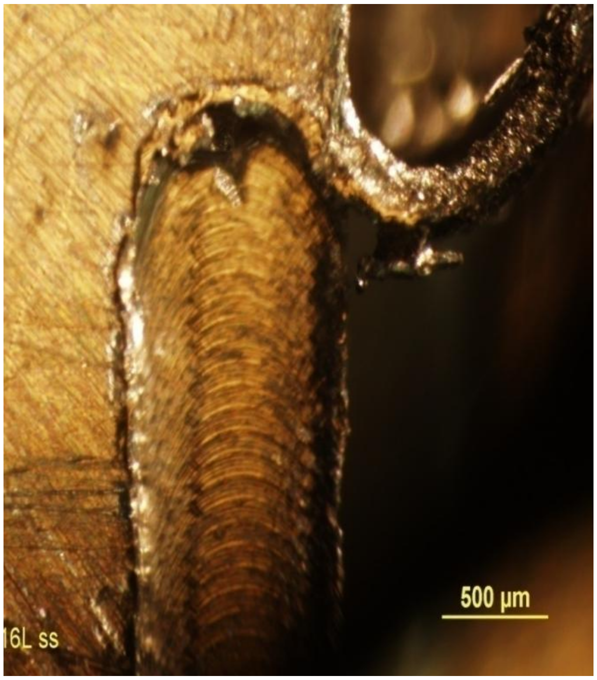

Figure 28. 316L stainless steel block from crash test showing where the tool failed. (N=6,000 rpm, f_c =76 µm/tooth, depth of cut =0.7 mm, width of cut=0.59mm)

Figure 29 shows the SEM image of the surface of microtool failed in the crash tests. The granules of tungsten carbide clearly suggest the brittle fracture of the tool.

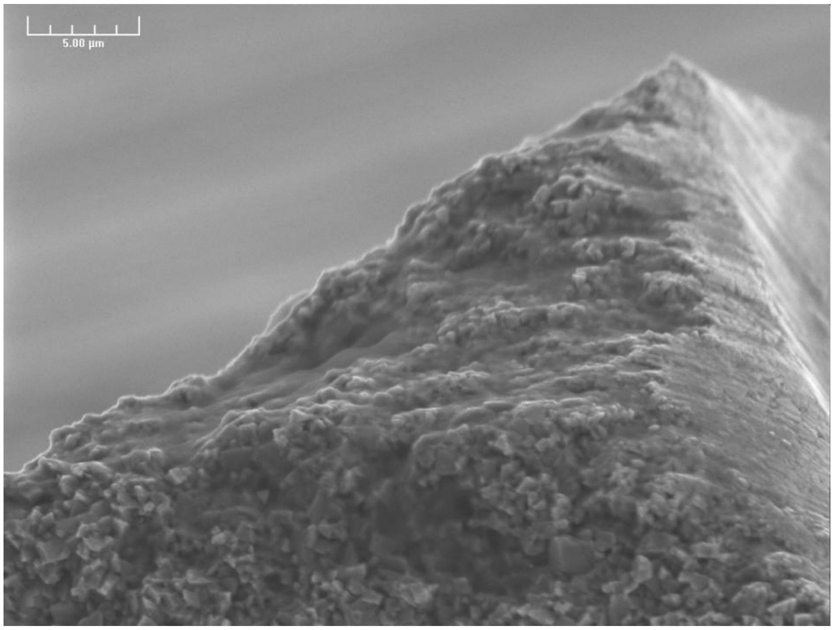

Figure 29. SEM image of the tungsten carbide tool from crash test showing brittle failure

Table 11 shows the shear force (F_s) calculated form equation (1) of section 4.1. The distance 'b' was measured after the crash tests. Sample calculation for shear force was explained in Appendix (B1). The shear force values for larger depth of cut are clearly higher than the corresponding shear force values at smaller depth of cut due to increase in shear area of cut. The axial depth of cut of 0.35 mm corresponds to 17.25% of the cutter length and axial depth of 0.70 mm corresponds to 34.5% of cutter length.

Table 11. Shear force from crash tests for N= 6,000 rpm and cutting speed = 19.1m/sec

Experiment #	Axial depth of cut (h), mm	Feed per tooth (f_c) , μm/tooth	Distance where the tool failed (b), mm	Shear force (F_s), N
1	0.35	38	23.7	126.43
2	0.35	38	20.9	109.26
3	0.35	76	14.23	78.50
4	0.35	114	11.71	66.72
5	0.35	152	6.62	43.91
6	0.70	38	16.11	175.73
7	0.70	76	14.69	160.70
8	0.70	114	10.15	121.14
9	0.70	152	5.38	76.40

Tables 12 and 13 show the cutting force in the feed direction (F_c) obtained from crash test using equation (3) from section 4.1. The crash tests were performed with Rustlick WS-500 A flood coolant but the analysis was extended to observe the cutting force on the tool for different coolant conditions. The coefficient of friction (μ) values for dry cutting conditions to greasy conditions when machining tungsten carbide tool with 316L SS workpiece were considered. The 'μ' values range from 0.08-0.19 for greasy cutting conditions to dry cutting conditions for machining tungsten carbide tool on 316L SS workpiece (Beardmore 2008).

Table 12. Cutting force from crash tests for depth of cut = 0.35 mm, μ = 0.08-0.19 (Beardmore 2008), f_c = 38 μm/tooth- 152 μm/tooth

Coefficient of Friction (μ)	Shear angle (ϕ)	Cutting force (F_c), N For Fs=126.43N f_c = 38 μm/tooth	Cutting force (F_c), N For Fs=109.26N f_c = 38 μm/tooth	Cutting force (F_c), N For Fs=78.50N f_c = 76 μm/tooth	Cutting force (F_c), N For Fs=66.72N f_c = 114 μm/tooth	Cutting force (F_c), N For Fs=43.91N f_c = 152 μm/tooth
0.08	46.73	173.38	149.84	107.66	91.49	60.21
0.09	46.45	174.29	150.62	108.22	91.97	60.53
0.10	46.17	175.20	151.41	108.79	92.45	60.84
0.11	45.88	176.10	152.19	109.34	92.93	61.15
0.12	45.60	176.99	152.96	109.90	93.40	61.46
0.13	45.32	177.88	153.72	110.45	93.87	61.77
0.14	45.04	178.76	154.48	111.00	94.33	62.08
0.15	44.76	179.63	155.24	111.54	94.79	62.38
0.16	44.48	180.50	155.99	112.08	95.25	62.68
0.17	44.20	181.36	156.73	112.61	95.70	62.98
0.18	43.92	182.21	157.47	113.14	96.15	63.28
0.19	43.64	183.06	158.20	113.66	96.60	63.57

Table 13. Cutting force from crash tests for depth of cut = 0.70 mm, µ = 0.08-0.19 (Beardmore 2008), f_c = 38 µm/tooth- 152 µm/tooth

Coefficient of friction (μ)	Shear angle (ϕ)	Cutting force (F_c), N For Fs=175.73N f_c = 38 µm/tooth	Cutting force (F_c), N For Fs=160.63N f_c = 76 µm/tooth	Cutting force (F_c), N For Fs=121.14N f_c = 114 µm/tooth	Cutting force (F_c), N For Fs=76.40N f_c = 152 µm/tooth
0.08	46.73	240.99	220.38	166.12	104.78
0.09	46.45	242.26	221.54	166.99	105.33
0.10	46.17	243.52	222.69	167.86	105.87
0.11	45.88	244.77	223.84	168.72	106.42
0.12	45.60	246.01	224.97	169.58	106.96
0.13	45.32	247.24	226.10	170.43	107.49
0.14	45.04	248.47	227.22	171.27	108.03
0.15	44.76	249.68	228.33	172.11	108.55
0.16	44.48	250.89	229.43	172.94	109.08
0.17	44.20	252.08	230.52	173.76	109.60
0.18	43.92	253.27	231.61	174.58	110.11
0.19	43.64	254.44	232.68	175.39	110.62

Sample calculation of cutting force can be found in Appendix (B1). Increase of cutting force with increase in axial depth of cut for corresponding chip load can be observed in Tables 12 and 13. The increase in cutting force with increase in depth of cut clearly shows the effect of shear area on the cutting force.

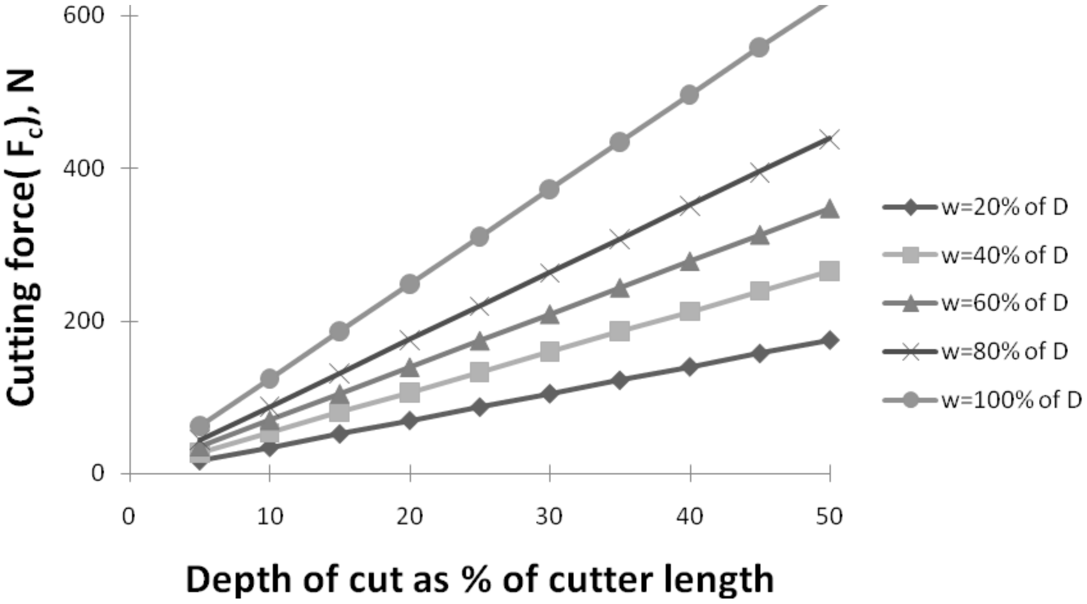

Figure 30. Cutting force for axial and radial depths of cut when machining 316L stainless steel. (f_c= 38 µm/tooth and µ=0.19)

Figure 30 shows the cutting force acting on the tool in feed direction with axial depth of cut as percentage of cutter length and width of cut as percentage of tool diameter from the force model developed in section 4.1. The cutting force increases clearly with increase in axial and radial depths of cut. The predicted cutting force calculated can be used to understand the effect of cutting force acting on the microtool for different cutting conditions.

Bao et al. (2001 a) reported that the maximum cutting force in feed direction for machining a NAK 55 steel using 3.175 mm (0.125 in) two flute carbide end-mill, with cutting conditions of 2,000 rpm spindle speed, 25.4 mm/min (1 in/min) feed rate, 0.0625 mm width of cut and 0.0625 mm axial depth of cut. The current research employs extreme cutting conditions of feed rate upto 1828.8 mm/min (72 in/min) to estimate the cutting forces and understand tool failure. The spindle speed of 6,000 rpm was used for machining and a higher feed per tooth upto 152µm/tooth was used to analyze the effect of extreme conditions on microtool.

5.3.1 EFFECT OF CUTTER RUNOUT ON CUTTING FORCE

The effect of cutter runout on cutting force was studied to understand the significance of tool runout. The cutting force was considered in the extreme case of maximum friction coefficient (µ) equal to 0.19.

Table 14. Cutting force variation with tool runout for depth of cut = 0.35 mm, chipload (f_c) ranging from 38 µm/tooth- 152 µm/tooth and µ=0.19

Tool runout (e), µm	Coefficient of Friction (μ)	Cutting force (F_c), N For f_c = 38 µm/tooth	Cutting force (F_c), N For f_c = 76 µm/tooth	Cutting force (F_c), N For f_c = 114 µm/tooth	Cutting force (F_c), N For f_c = 152 µm/tooth
0	0.19	183.06 158.20	113.65	96.57	63.57
5		183.11 158.24	113.68	96.59	63.60
10		183.17 158.27	113.71	96.62	63.63
15		183.23 158.31	113.73	96.65	63.67
20		183.28 158.35	113.76	96.68	63.70

Table 15. Cutting force variation with tool runout for depth of cut = 0.70 mm, chipload (f_c) = 38 µm/tooth- 152 µm/tooth and µ=0.19

Tool runout (e), µm	Coefficient of Friction (μ)	Cutting force (F_c), N For f_c = 38 µm/tooth	Cutting force (F_c), N For f_c = 76 µm/tooth	Cutting force (F_c), N For f_c = 114 µm/tooth	Cutting force (F_c), N For f_c = 152 µm/tooth
0	0.19	254.46	232.68	175.36	110.57
5		254.52	232.74	175.42	110.64
10		254.58	232.80	175.48	110.71
15		254.64	232.85	175.54	110.78
20		254.70	232.91	175.60	110.85

From Tables 14 and 15 the variation in cutting force with tool runout was observed to be in the range of 0.02%- 0.06%. The increase in cutting force can be observed with increase in tool runout. The cutting force variation values were lower due to higher chipload relative to tool runout used in the crash tests.

The amount of work done by the cutting tool was calculated from the crash tests. This data helps in understanding the energy lost by the microtool during machining. From Table 14, for chipload f_c of 38 µm/tooth the variation in cutting force was observed to be approximately + 10N from the average value. Considering this variation of cutting force and chipload for each experiment the work done was calculated and plotted against the number of tool revolutions until tool failure.

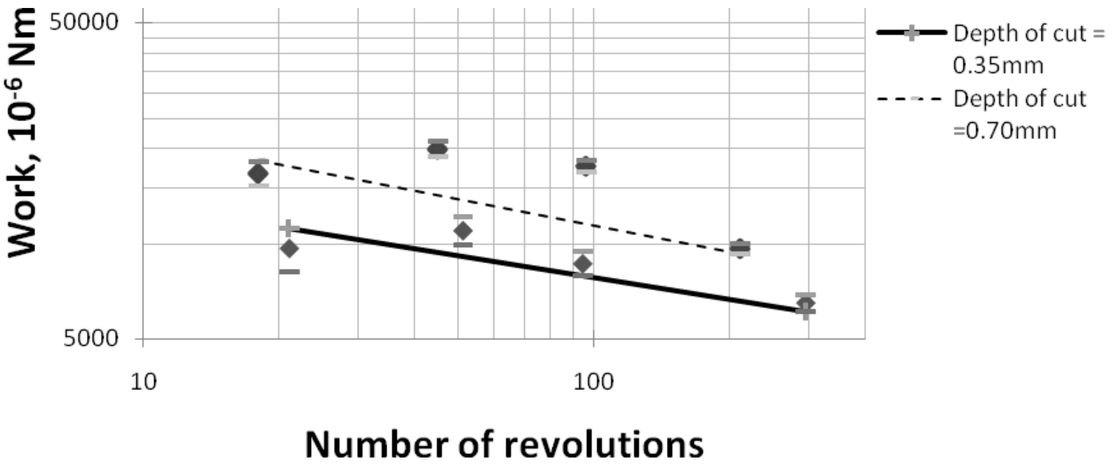

Figure 31. Work done vs number of revolutions until tool failure (Axial depth of cut = 0.35 mm and 0.7 mm, μ = 0.19, (f_c) = 38 μm/tooth- 152 μm/tooth.)

From Figure 31 it was observed that for higher chiploads the work done by the tool was higher and the tool failed for lower number of revolutions. Clearly from both the figures decrease in work done by the tool increased the life of the tool. Figure 31 explains the premature failure of microtool for higher chipload for any combination of chipload and cutting force greater than the threshold values.

5.3.2 FRICTION AREA AND EFFECT OF TOOL RUNOUT ON FRICTION AREA

The equations (8), (9) and (10) formulated in section 4.2 were used to study the friction area resulted from the crash test for different cutting conditions.

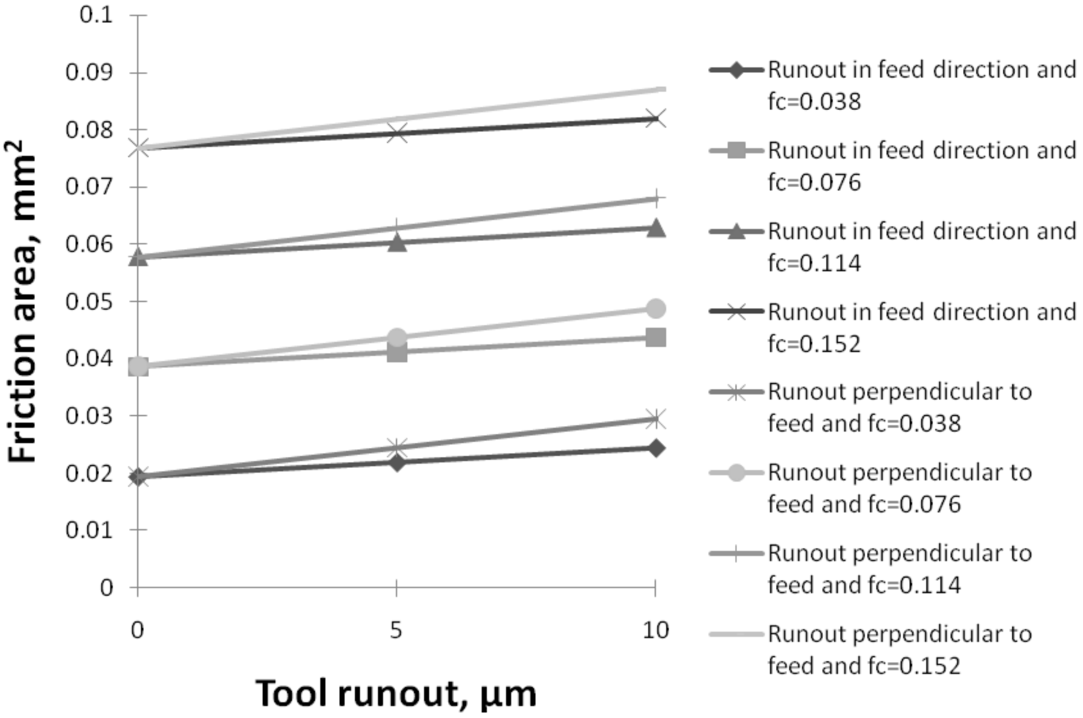

Figure 32. Friction area formulated for tool runout along and normal to feed direction, f_c = chipload, µm/tooth

Figure 32 shows the friction area calculated with tool runout. The additional friction areas for tool runout in direction of feed (A_{r1}) and for runout perpendicular to feed (Ar2) were calculated using the model. The increase in friction area was observed with increase in chipload (f_c). Figure 32 shows the increase in friction area with increase in runout (e). The additional friction area with runout perpendicular to feed (A_{r2}) increases with tool runout (e) but is independent of chipload (f_c). The additional friction area with runout in the direction of feed increases with increase in both runout and chipload.

The increase in tool runout would affect the tool by increase in friction force acting on the tool and hence reduces the performance of the tool. The tool has to impart higher energy, to cut the increased area due to runout and thereby losing its efficiency. Hence the model to calculate the friction area helps to understand the effect of cutter runout on the microtool.

5.4 SPECIFIC CUTTING ENERGY ESTIMATION FROM CUTTING FORCE

The equations (11) through (13) discussed in section 4.3 were used to estimate the specific energy for cutting of 316L stainless steel from the cutting force data obtained from the crash tests. From Tables 12 and 13 the cutting force values at coefficient of friction (µ) equal to 0.19 was considered to estimate the specific energy. Tables 16 and 17 show the results obtained for specific cutting energy estimated with the cutting force obtained for depth of cut of 0.35 mm and 0.7 mm respectively.

Table 16. Specific cutting energy estimated from cutting force in feed direction for µ= 0.19 and depth of cut =0.35 mm

	Feed per tooth, $f_{c} = 38$ µm/tooth	Feed per tooth, $f_{c} = 76$ µm/tooth	Feed per tooth, $f_{c} = 114$ µm/tooth	Feed per tooth, $f_{c} = 152$ µm/tooth
Cutting force F_{c}, N	183.06	113.66	96.60	63.57
	158.20			
Specific energy u, J m^{-3} x 10^{8}	196.49	71.77	44.10	23.06
	173.94			

Table 17. Specific cutting energy estimated from cutting force in feed direction for μ= 0.19 and depth of cut =0.70 mm

	Feed per tooth, f_{c} = 38 µm/tooth	Feed per tooth, f_{c} = 76 µm/tooth	Feed per tooth, f_{c} = 114 µm/tooth	Feed per tooth, f_{c} = 152 µm/tooth
Cutting force F_{c},N	254.44	232.68	175.39	110.62
Specific energy u, J m^{-3} x 10^{8}	139.8	73.4	40.4	20.06

The approximate value of specific energy for stainless steel (18-8) from table 8 is given as 49.14x10^{8} J m^{-3}. The difference in specific energy calculated from the cutting force obtained in crash tests and the value provided by Shaw (2005) can be accounted to the approximations involved in the specific energy calculations for a given rake angle and chipload.

5.5 FINITE ELEMENT ANALYSIS OF CUTTING TOOL

Finite element analysis was performed on the microcutting tool modeled in SolidWorks. Linear static analysis was performed for different cutting conditions to study the effect of cutter displacement and cutting force on tool failure. The tool displacement and the cutting force were used as boundary conditions for the analysis of the cutting tool. Parabolic tetrahedral solid elements shown in Figure 33 were used for meshing. The parabolic elements have an advantage over linear elements as they represent curved boundaries more accurately, and produce better mathematical approximations. Figure 34 shows the cutting tool model used for the analysis.

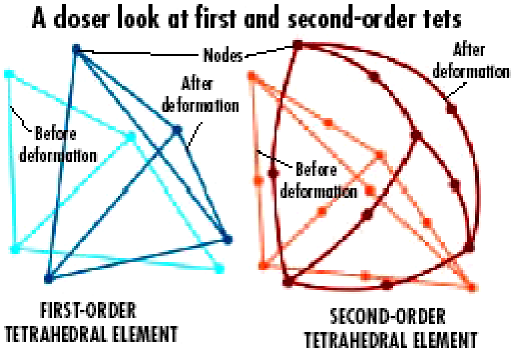

Figure 33. First and second-order tetrahedral elements before and after deformation (Penton Media, 2004)

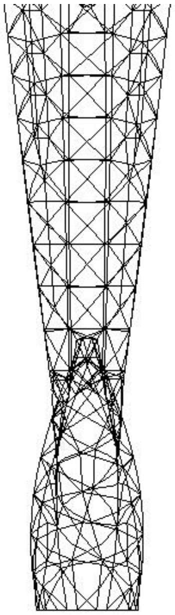

Figure 34. Meshed tool model used for finite element analysis of microend-mill

5.5.1 FINITE ELEMENT ANALYSIS FOR TOOL DEFLECTION

Finite element analysis was performed to study the effect of tool deflection on cutting tool. The maximum tool deflection of 20 µm from micromachining at 25,000 rpm was used to study the stress distribution on the tool while machining. Figure 35 shows the maximum stress areas on the cutting tool for the applied displacement. The critical high stress areas were observed at the end of the cutter. The maximum stress in the microtool for 20 µm tool deflection (2% tool diameter) was found to be 1.6% of the flexure strength of cutting tool.

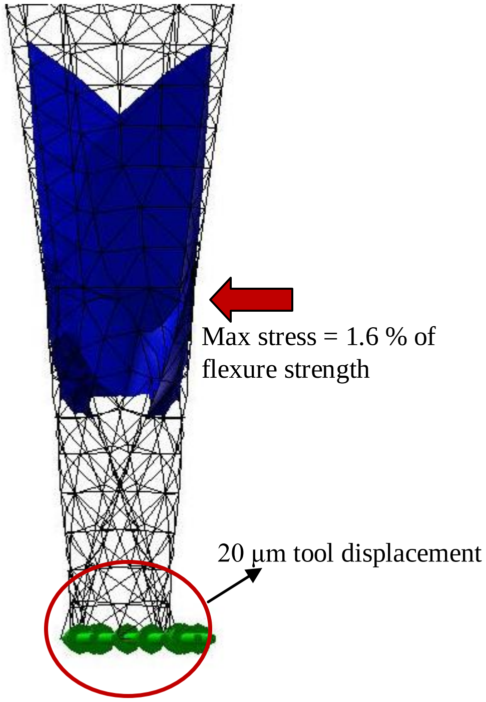

Figure 35. Stress profile for a tool deflection of 20 µm at the tool tip
(f_c =10 µm, N= 25,000 rpm)

5.5.1.1 MAXIMUM DEFLECTION CAUSING MAXIMUM STRESS

The finite element model was further analyzed to study the tool deflection that would cause a maximum stress close to the flexure strength of the microtool. This data would help to understand the extreme deflections that would result in tool failure. The analysis was performed for stress value equal to 50% of the flexure strength of material and 100% of flexure strength of the microtool.

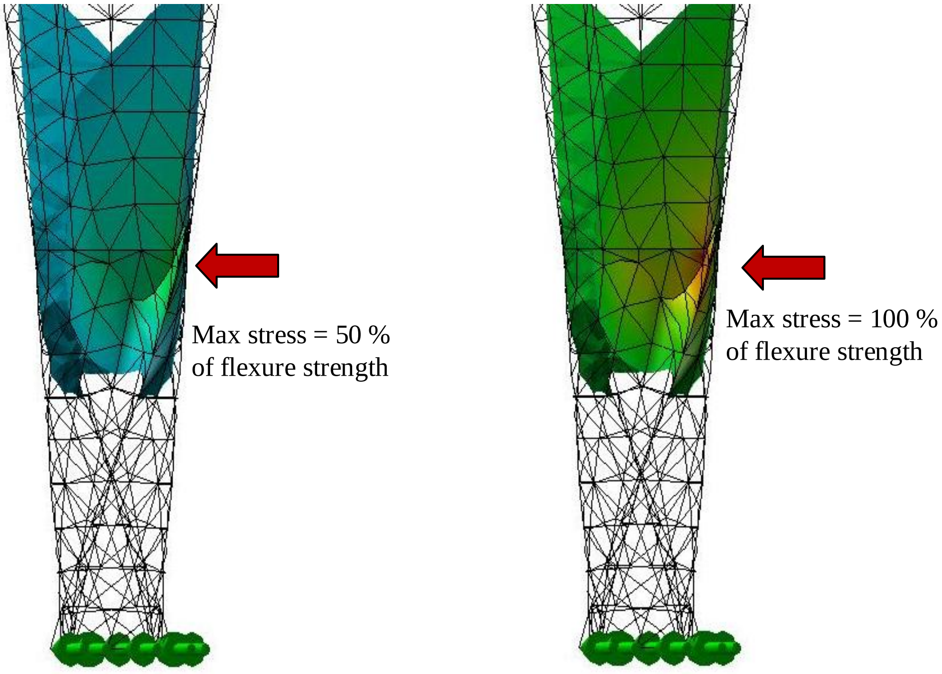

(a) (b)

Figure 36. Stress distribution for tool deflection causing
(a) Maximum stress in tool is 50% of flexure strength for tool deflection of 0.49 mm
(b) Maximum stress in tool is 100% of flexure strength for tool deflection of 1.01 mm

Figure 36 shows the stress distribution in the microtool for 50% and 100% of flexure strength of the tool due to tool deflection. Clearly for both the cases the maximum stress area is observed at the end of the cutter. The maximum deflections corresponding to both the cases were equal to 0.49 mm and 1.01 mm respectively. The deflections 0.49 mm and 1.01 mm correspond to 48% of cutter diameter and 99% of cutter diameter. Table 18 consolidates the maximum stress observed in the tool based on tool deflection.

Table 18. Tool deflection and maximum stress predicted by finite element analysis of Ø1.016 mm x 2flute tungsten carbide endmill.

Tool deflection, mm	Maximum stress, % Flexural strength
0.02	1.6%
0.49	50%
1.01	100%

5.5.2 FINITE ELEMENT ANALYSIS FOR CUTTING FORCE

Finite element analysis was performed on the cutting tool to study the effect of cutting force to predict the failure of the tool. The cutting force was applied on the cutting tool for different axial depths of cut used in the crash tests. The maximum cutting force for the tool failure was predicted based on the maximum normal stress criteria for brittle materials. Further the effect of tool rotation was observed by applying the cutting force along different angles of rotation of tool and analyzing the maximum stress values. The finite element analysis was also extended to study the effect of maximum cutting force acting along the length of cutter and maximum cutting force acting as a point load on the cutting tool.

5.5.2.1 CUTTING FORCE ALONG 17.25% OF CUTTER LENGTH

The maximum amount of force that would fail the tool for depth of cut of 17.25% of cutter length was measured using finite element analysis. The boundary condition was applied as the cutting force acting on the microtool in the direction of feed for the given depth of cut. Figure 37 (a) shows the application of cutting force along the cutter for axial and radial depth of cut equal to 17.25% of cutter length and 0.26mm respectively. The planes in figure 37 (b) were used to study the effect of orientation of cutting force during cutting.

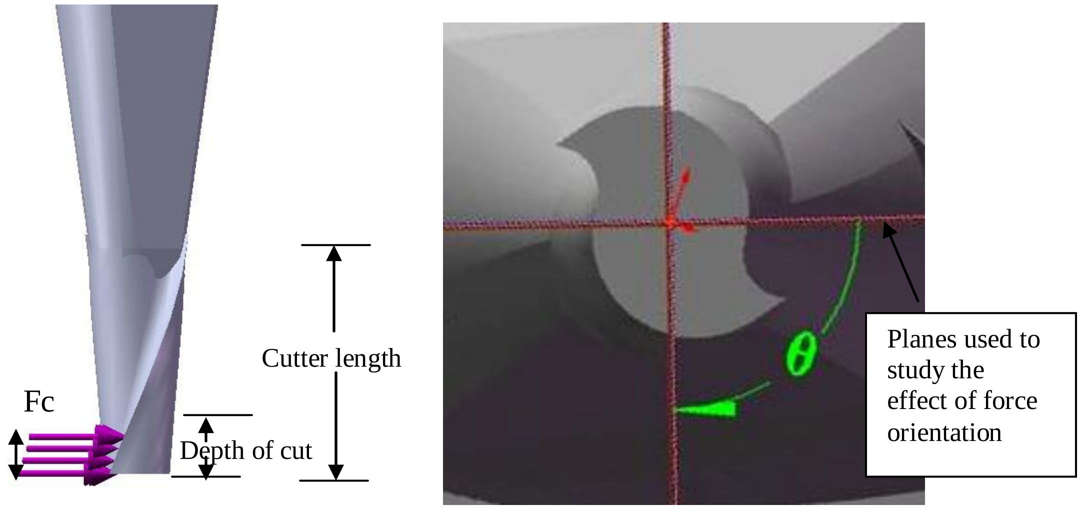

(a) (b)

Figure 37. FEA model of cutting tool showing cutting force
(a) Cutting force acting on 17.25% of its cutter length
(b) Different planes to study the effect of cutting force orientation

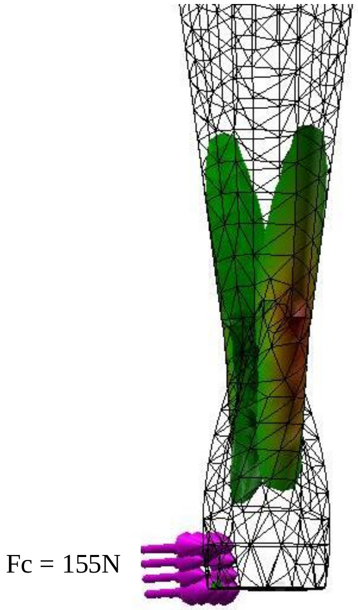

Figure 38. Stress profile of critical areas of failure for cutting force of 155N for 17.25% of cutter length

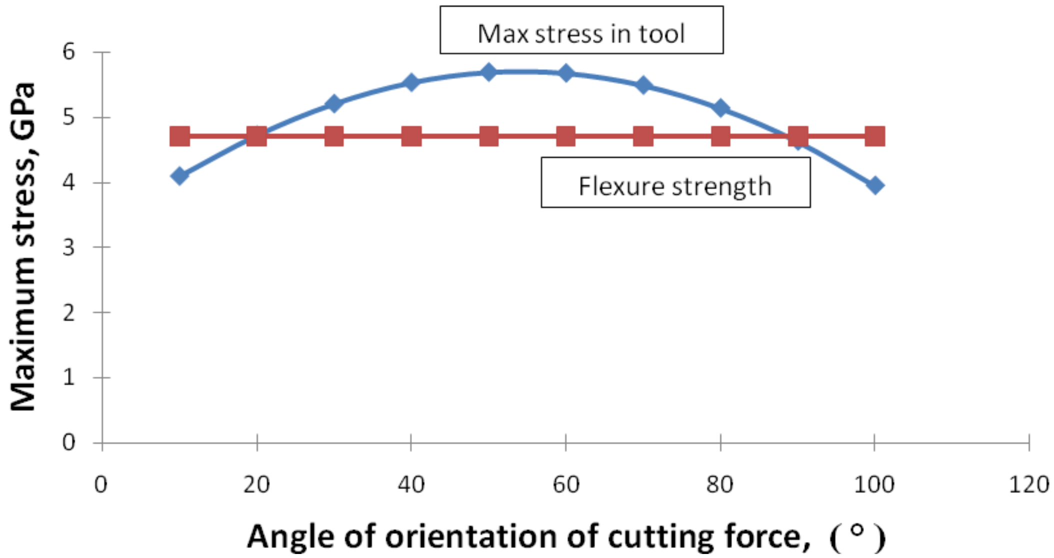

Figure 39. Effect of tool rotation on the maximum stress caused in the tool for a constant cutting force of 155N

Figure 38 shows the maximum cutting force from finite element analysis of the cutting tool for an axial depth of cut of 17.25% of cutter depth was equal to 155 N. The critical areas of high stress were observed at the end of the cutter. The tool failure starts at these high stress areas when the cutting force exceeds the flexure strength of tool. The value of 155 N obtained from FEA is in accordance with the cutting force obtained from in the section (5.3), which notes that the cutting force acting on the tool for a depth of cut equal to 17.25% of cutter length is in the range of 150 N to 185 N for lower chiploads. Figure 39 shows that for a distributed force of 155N the maximum stress is observed when the cutting force acts in between 40- 60 degrees to feed direction.

5.5.2.2 CUTTING FORCE ALONG 34.50% OF CUTTER LENGTH

The maximum amount of force that would fail the tool for depth of cut of 34.5% of cutter length was measured using finite element analysis. The boundary condition was applied as the cutting force acting on the microtool in the direction of feed for the given depth of cut. Figure 40 shows the application of cutting force along the cutter for a depth of cut equal to 34.5% of cutter length and radial depth of cut equal to 0.26 mm. The approach similar to Figure 37 (b) was used to study the effect of tool rotation during cutting.

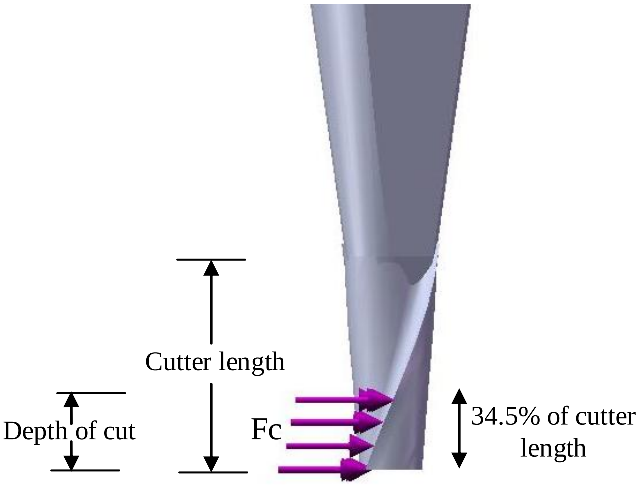

Figure 40. FEA model of cutting tool showing cutting force acting on 34.5% of cutter length

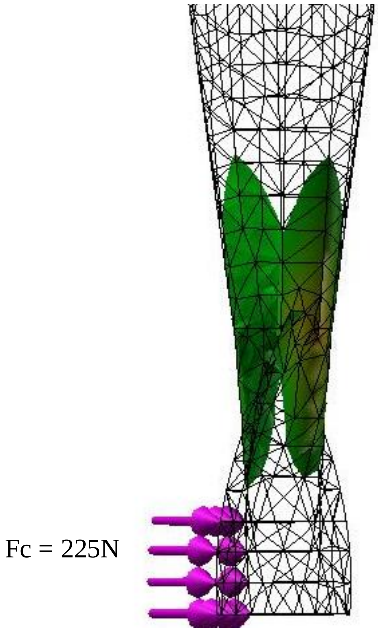

Figure 41. Stress profile of critical areas of failure for a cutting force of 225N for 34.5% cutter length

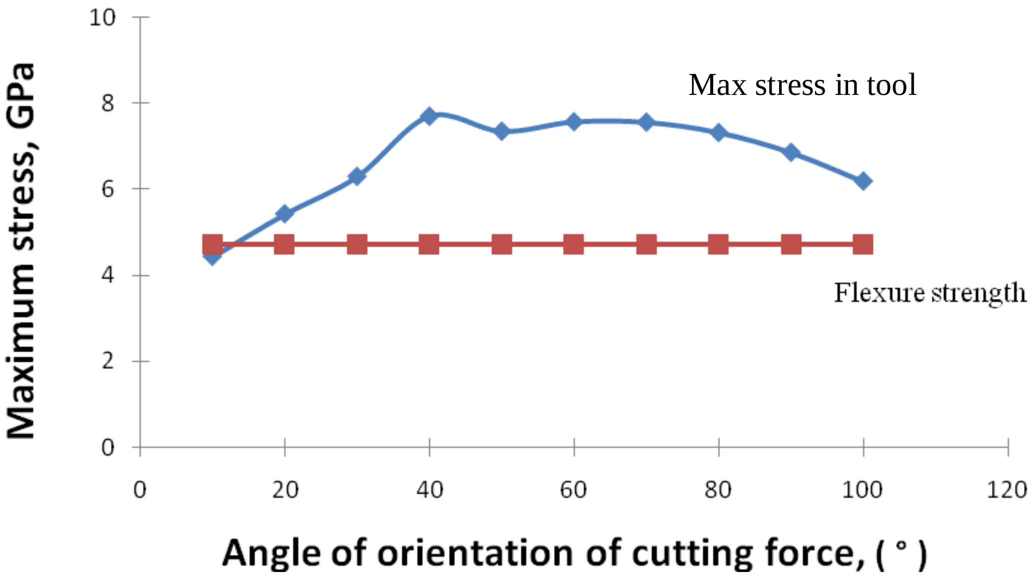

Figure 42. Effect of tool rotation on the maximum stress caused in the tool for a constant cutting force of 225N

Figure 41 shows the maximum cutting force from finite element analysis of the cutting tool for an axial depth of cut of 34.5% of cutter depth was equal to 225 N. The critical areas of high stress were observed at the end of the cutter. The tool failure starts at these high stress areas when the cutting force exceeds the flexure strength of tool. The value of 225 N obtained from FEA is in accordance with the cutting force obtained from crash tests where the cutting force obtained for lower chipload is equal to 220 N to 240 N. Figure 42 shows that for a distributed force of 225N the maximum stress is observed when the cutting force acts in between 45- 60 degrees to feed direction.

5.5.2.3 CUTTING FORCE ACTING ALONG THE CUTTER LENGTH

The analysis was extended to study the effect of maximum amount of cutting force in feed direction that would fail the tool for depth of cut equal to the cutter length. Figure 43 shows FEA model with cutting force acting on the entire cutter length. This analysis would help to understand the maximum force that could be exerted on the cutting tool during the machining process. The maximum force is measured based on the maximum normal stress criteria of brittle materials.

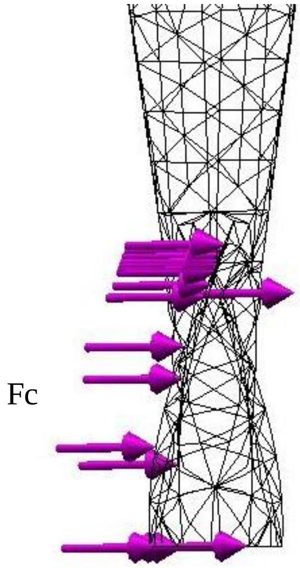

Figure 43. FEA model of cutting tool with cutting force acting on entire cutter length

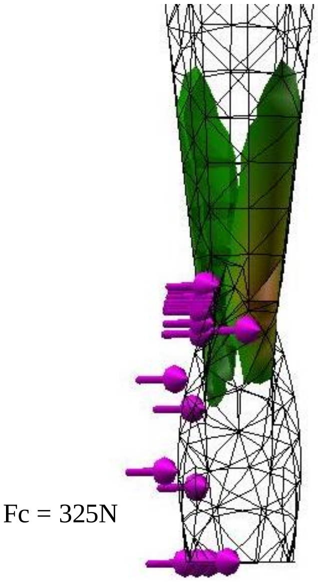

Figure 44. Stress profile of critical areas of failure for a cutting force of 325N for 100% of cutter length

The FEA of the tool based on above criteria suggested that the maximum distributed force that can act on the tool at which the tool fails is equal to 325N. Figure 44 shows the critical areas of high stress due to the force acting on the cutter due to the applied cutting force. Figure 44 explains the high stress areas on the tool that would result in tool failure during the machining process. This location of high stress points on the tool for the cutting force acting on the cutter are in coherence with those obtained when the cutting force acts on part of the cutter.

5.5.2.4 CUTTING FORCE ACTING AS A POINT LOAD ON THE CUTTER

Figure 47 shows the stress distribution obtained from finite element analysis of tool for cutting force acting as a point load. The tool fails at a cutting force of 40 N. The stress profile in figure 45 due to point load shows high stress areas at tool tip suggesting tool chip off.

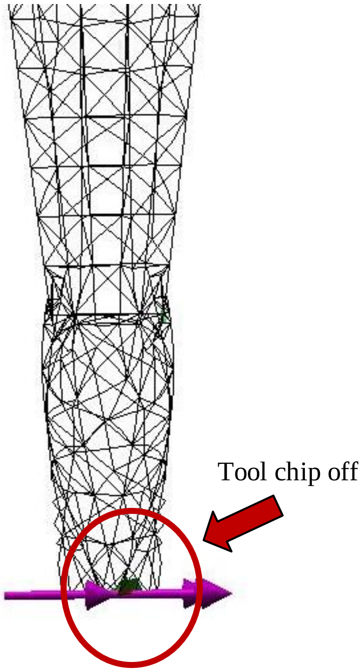

Figure 45. Stress profile showing tool chip off for a point load of 40N

Figure 46 shows the cutting force in feed direction that would result in tool failure predicted by finite element analysis for cutting force distributed along the length of cutter. The increase in cutting force was clearly observed with increase in depth of cut.

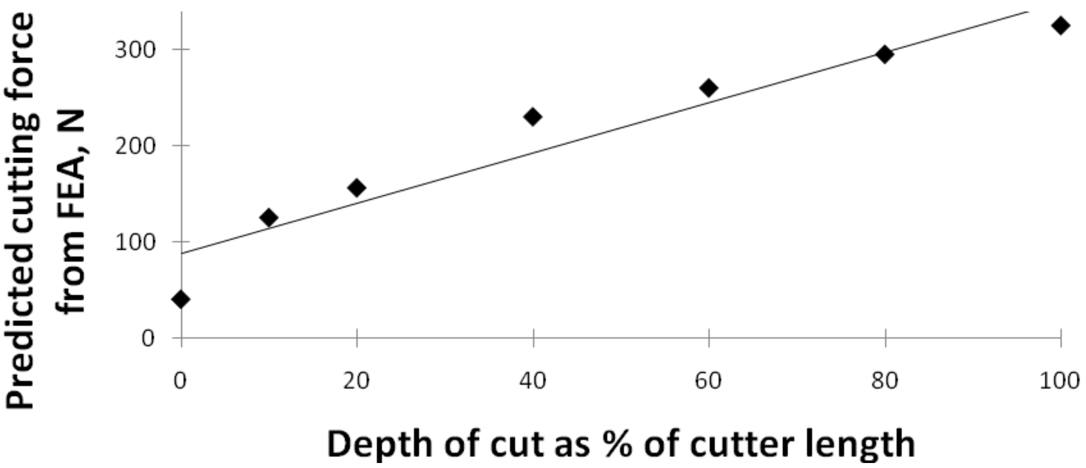

Figure 46. FEA prediction of cutting force resulting in tool failure as % of cutter length

Table 19 compares the cutting force data obtained from different techniques used in the research. Cutting force was calculated by the force model developed by Bao et al. (2000a) using correction factor suggested for f_c/R greater than 0.1 as shown in Figure 47.

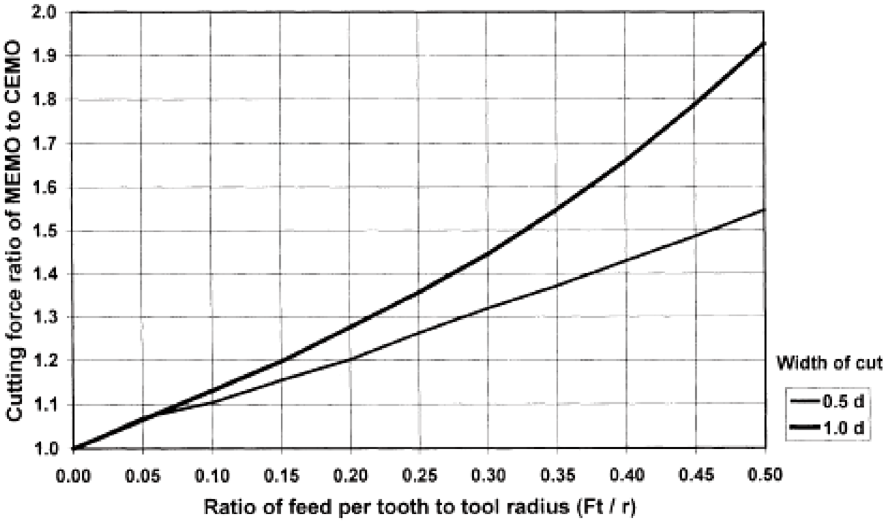

Figure 47. Difference of feed direction cutting force between Bao force model and conventional force models. (Bao et al. 2000a)

Table 19. Cutting force comparison from different techniques

Axial depth of cut, mm	Measured radial depth of cut, mm	Chip load, µm/tooth	Cutting force (Fc) that would result in tool failure, N		
			Shear µ=0.19	FEA	Bao model
0.35	0.95	38	183.06	-	69.6
0.35	0.84	38	158.20	-	71.6
0.35	0.57	76	113.66	-	148.8
0.35	0.47	114	96.60	-	199.9
0.35	0.26	152	63.57	155	241.0
0.7	0.64	38	254.66	-	101.3
0.7	0.59	76	232.68	-	192.7
0.7	0.41	114	175.39	-	270.3
0.7	0.22	152	110.62	225	308.0

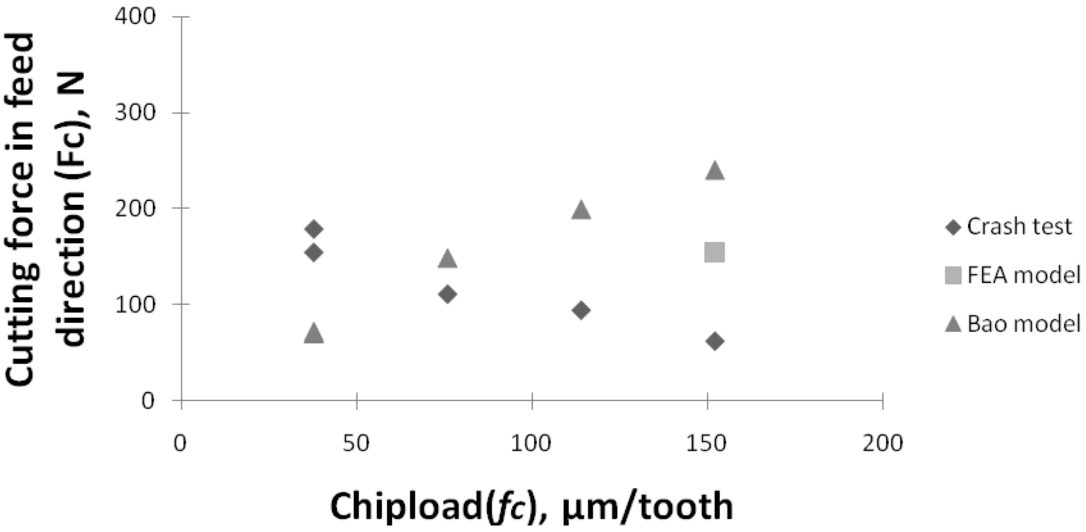

Figure 48. Cutting force comparison from different techniques for axial depth of cut = 0.35 mm

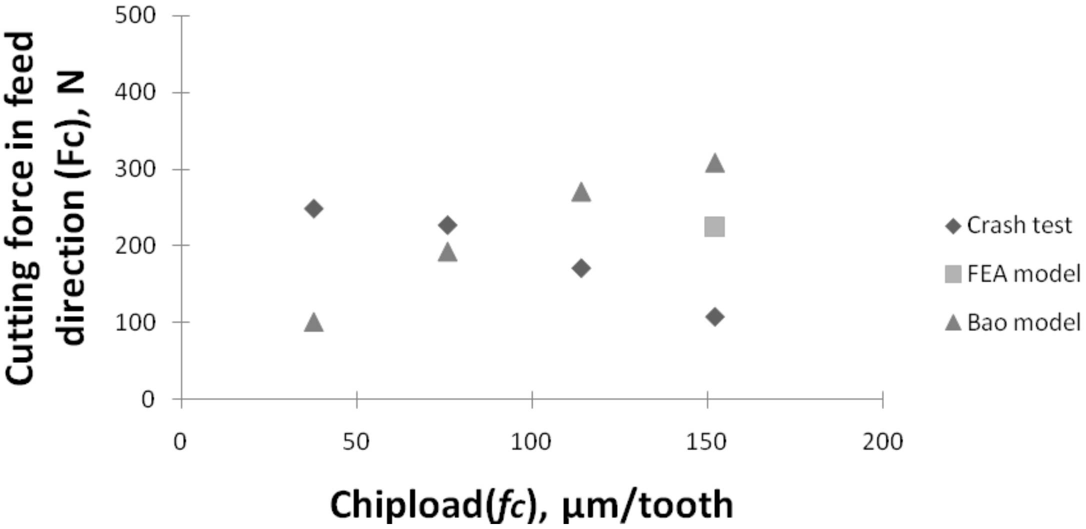

Figure 49. Cutting force comparison from different techniques for axial depth of cut = 0.70 mm

Figures 48 and 49 represent the cutting force data obtained as function of chipload using different techniques for different axial depths of cut. The cutting force values calculated from crash tests, by measuring shear area, were in close agreement with force values predicted using FEA values and force model developed by Bao et al. (2000a) for lower values of chipload. At higher chipload values, close to conventional machining values, the chipload to cut diameter is very high and the tool fails at very low values of cutting force right at the start of machining. The failure at higher chipload can be explained from Figures 32 and 33 where the higher work done resulted in tool failure for lower number of revolutions.

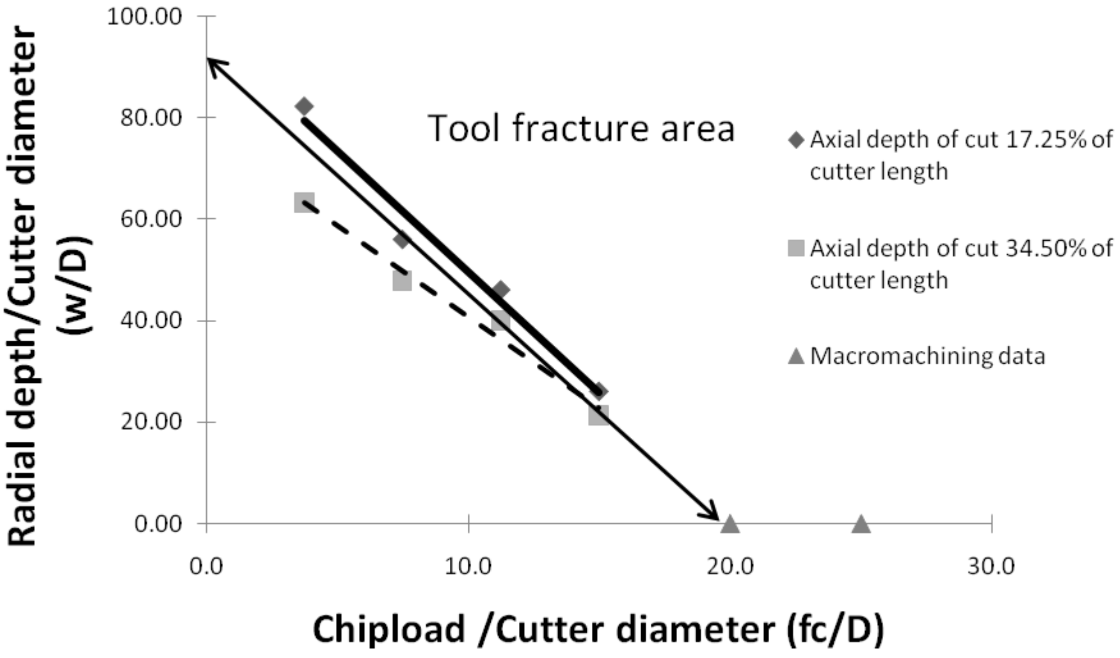

Figure 50. Maximum cutting conditions for failure of microcutting tool as function of radial and axial depths of cut, and chipload. (f_c – chipload, w- radial depth of cut, D- cutter diameter)

Figure 50 can be used to obtain the cutting conditions to prevent the tool failure for axial depths of cut equal to 17.25% of cutter length and 34.5% of cutter length. Any combination of cutting conditions above the plot would result in tool failure. The cutting conditions of chipload and radial depth of cut as a percentage of cutter diameter can be obtained from Figure 50 and these cutting conditions can be used to predict the tool failure.

6. CONCLUSIONS

A novel method to predict microtool failure was developed:

1. Microtool fails due to eccentric rotation and cyclic loading. Measure of microtool runout and deflection during machining using laser, shows a tool runout less than 1 µm and tool deflection of 20 µm when machining at 25000 rpm spindle speed.
2. Finite element analysis (FEA) predicts tool failure due to static bending for a deflection greater than 99% of tool diameter.
3. The difference of cutting force estimations from shear area measurement, finite element analysis and available theory were in the range of 25% - 48% for chipload equal to 15% of cutter diameter.
4. Work done (cutting force x chipload) by cutting tool can be used to predict tool failure. Any combination of cutting force and chipload greater than threshold values would result in tool failure.
5. FEA predicts maximum stress for cutting force oriented between 45-60 degrees to feed direction.
6. Cutting conditions to predict tool failure were suggested for axial depths of cut in the range of 17.25% - 34.5% of cutter length. Any combination of chipload and radial depth of cut greater than threshold values would result in tool failure. For a chipload greater than 20% of cutter diameter the microtool fails instantly for any radial depth of cut.

7. RECOMMENDATIONS

The future work can be extended following the recommendations:

1. Measure force directly using a sensitive dynamometer
2. Extend to microdrilling
3. Measure friction between cutting tool and workpiece

REFERENCES

ASTM Standard A240. (2007). “Specification for chromium and chromium-nickel stainless steel slate, sheet, and strip for pressure vessels and for general applications.” *ASTM International*, West Conshohocken, PA. http:// www.astm.org/. Access date 01/05/2009.

AZoM™, Pty.Ltd. (2009). “Grade 316L – properties, fabrication and applications.” http://www.azom.com/Details.asp?ArticleID=2382. Access date 01/05/2009.

Bao, W.Y. and Tansel, I.N. (2000a). “Modeling microend-milling operations. Part I: analytical cutting force model.” *International Journal of Machine Tools & Manufacture* (v40), pp2155–2173.

Bao, W.Y. and Tansel, I.N. (2000b). “Modeling microend-milling operations. Part II: tool run-out.” *International Journal of Machine Tools & Manufacture* (v40), pp 2175–2192.

Beardmore, R. (2008). “Coefficients of friction.” http://www.roymech.co.uk/Useful_Tables/Tribology/co_of_frict.htm. Access date 01/05/2009.

Byrne, G.; Dornfeld, D.; and Denkena, B. (2003), “Advancing Cutting Technology.” *Annals of the CIRP* (**v**52/2), pp483–507.

Dharnorker, A. and Ozel, T. (2008). “Meso/micro scale milling for micromanufacturing.” *International Journal of Mechatronics and Manufacturing Systems* (v1), pp 23 – 42.

Fang, F.Z.; Wu, H.; Liu, X.D.; Liu, Y.C.; and Ng, S.T. (2003). "Tool geometry study in micromachining" *Journal of Micromechanics and Microengineering* (v13), pp726–731.

Friedrich, C. and Vasile, M. (1996). "The micromilling process for high aspect ratio microstructures." *Microsystem Technology* (v2, n3), pp144–148.

Gere, J. M. and Timoshenko, S. P. (1972). *Mechanics of Materials*. New York: Van Nostrand Reinhold.

Groover, M.P. (2004). *Fundamentals of Modern Manufacturing*. New York: John Wiley & Sons.

Goodman, L.S.; Mengelt, T.J.; Ali, M; Ulfig, R.M.; Istephanous, N; and Kelly, T.F. (2004). "Atomic structure and compositional analysis of 316L stainless steel medical device materials with the local electrode atom." *Microscopy and Microanalysis* (v2), pp1424-1425.

Haas Automation, Inc. (2009a). "Image of Haas VMC - office mills." http://www.haascnc.com/VMC_MODEL_OM.asp#VMCTreeModel. Access date 01/05/2009.

Haas Automation, Inc. (2009b). "Image of Haas VMC – 20IN." http://www.haascnc.com/VMC_MODEL_20IN.asp#VMCTreeModel. Access date 01/05/2009.

Keyence Corporation. (2009). "Image of LK-G157 laser specification." http://www.keyence.com/products/vision/laser/lkg/lkg_applications_4_1.php. Access date 01/05/2009.

Kim, C.J.; Mayor, J.R.; and Ni, J. (2004). “A static model of chip formation in microscale milling.” *Journal of Manufacturing Science and Engineering* (v126), pp710–718.

Kim, J.H.; Chang, H.K.; Han, D.C.; and Jang, D.Y. (2005). “Cutting force estimation by measuring spindle displacement in milling.” *Annals of the CIRP* (v54), pp67-70.

Kitahara, T.; Ishikawa, Y.; Terada, T.; Nakajima, N. and Furuta, K. (1996). “Development of micro-lathe.” *Mechanical Engineering Lab. Report, AIST/ MITI* (v50, n5), pp117–123.

Kline, W.A. and Devor, R.E (1983). “The effect of runout on cutting geometry and forces in milling.” *International Journal of Machine Tools and Manufacture* (v23), pp265-281.

Koenigsberger, F. and Sabberwal, A. J. P., (1961). “Chip section and cutting force during the milling operation,” *Annals of the CIRP* (v10), pp197-203

Konig, W.; Kutzner, K.; and Schehl, U. (1992). “Tool monitoring of small drills with acoustic emission.” *International Journal of Machine Tools and Manufacture* (v32), pp487-493.

Lee, K. and Dornfeld, D.A. (2004). "A study of surface roughness in the microend-milling process." *Laboratory for Manufacturing and Sustainability. Consortium on Deburring and Edge Finishing* . http://repositories.cdlib.org/lma/codef/kiha_03. Access date 01/05/2009.

Li, X.P. and Li, H.Z. (2004). “Theoretical modelling of cutting forces in helical end milling with cutter runout.” *Mechanical Sciences* (v46), (2004), pp1399–1414.

Liu, X.; DeVor, R.E.; Kapoor S.G.; and Ehmann, K.F. (2004). “The mechanics of machining at the microscale: assessment of the current state of the science.” *Journal of Manufacturing Science and Engineering, Transactions of the ASME* (v126, n4), pp666–678.

Lu, Z. and Yoneyama, T. (1999). "Micro cutting in the micro lathe turning system." *International Journal of Machine Tools and Manufacture* (v9), pp1171-1183.

M.A. Ford. (1998). “Carbide end mills.” http://www.maford.com/taf/catalog.taf?category=a13. Access date 01/05/2009.

Masuzawa, T and Toenshoff, H.K. (1997). “Three - dimensional micromachining by Machine Tools.” *CIRP Annals* (v46, n2), pp621–628.

Masuzawa, T. (2000). “State of the art of micromachining.” *CIRP Annals* (v49, n2), pp473–488.

McKeown, P.A. (1987). “The role of precision engineering in manufacturing of the Future.” *Annals of the CIRP* (v36), pp495-501.

MEMSnet. (2009). “Material: tungsten carbide (WC)” http://www.memsnet.org/material/tungstencarbidewcbulk/. Access date 03/05/2009.

Newby, G.; Venkatachalam, S.; and Liang ,S.Y. (2007). “Empirical analysis of cutting force constants in microend-milling operations.” *Journal of Materials Processing Technology* (v192–193), pp41–47.

Penton Media, Inc. (2004). “A closer look at model meshing.” http://machinedesign.com/ContentItem/61408/AcloserlookatModelMeshing.aspx. Access date 01/05/2009.

Ratner, B.D. (1996) *Biomaterials Science: An Introduction to Materials in Medicine.* San Diego: Academic Press.

Shaw, M. C. (2005). *Metal Cutting Principles.* Cambridge: MIT Press.

Stephenson, D. A. and Agapiou, J.S. (1997), *Metal Cutting Theory and Practice*. New York: Marcel Dekker, Inc.

Taniguchi, N. (1983). "Current status in, and future trends of, ultraprecision machining and ultrafine materials processing." *CIRP Annals* (v32, n2), pp573-582.

Tansel, I.; Rodriguez, O.; Trujillo, M.; Paz, E.; and Li, W. (1998). "Microend-milling-I. wear and breakage." *International Journal of Machine Tools & Manufacture*, (v38), pp1419–1436.

Tlusty J. and Macneil P. (1975). "Dynamics of cutting forces in end milling" *Annals of the CTW* (v24), pp21-25.

Tony, L. S.; Jeremiah, C.; Eric, M.; Nathan M.; and Duke, H. (2007). "Runout effects in milling: surface finish, surface location error, and stability." *International Journal of Machine Tools & Manufacture* (v47), pp 841–851.

Uhlmann, E. and Schauer, K. (2005). "Dynamic load and strain analysis for the optimization of microend mills." *CIRP Annals* (v54, n1), pp75-78.

Unist, Inc. (2007). "uni-MAX Coolubricator system." http://www.unist.com/machinecutting/MQL/Continuous_External/uniMAXcoolubricator.htm. Access date 01/05/2009.

Vasile, M. J.; Friedrich, C. R.; Kikkeri, B.; and Mcelhannon, R. (1996). “Micrometer-scale machining: tool fabrication and initial results.” *Precision Engineering,*(v19), pp 180–186.

Volger, M.P.; DeVor, R.E.; and Kapoor, S.G. (2004). “On the modeling and analysis of machining performance in microend-milling. Part II. Cutting force prediction, *Transactions of the American Society of Mechanical Engineers* (v126), pp 695–705.

Weule, H.; Huntrup, V.; and Tritschle, H. (2001). “Microcutting of steel to meet new requirements in miniaturization.” *CIRP Annals* (v50), pp61–64.

Yamagata, Y.; Mihara, S.; and Higuchi, T. (1995). “Microparts fabrication by ultra precision cutting technique.” *Proceedings of the 72nd JSME Spring Annual Meeting* (v95-1), pp242–245.

Zhou, M.; Yuan, Z.J.; and Dong, S. (2005). “Effect of diamond tool sharpness on minimum cutting thickness and cutting surface integrity in ultra-precision Machining.” *Journal of Materials Processing Technology* (v62), pp327–330.

APPENDIX A

PROPERTIES AND SPECIFICATIONS OF MATERIAL AND EQUIPMENT

A.1. 316L STAINLESS STEEL PROPERTIES

Table A-1. Physical properties of 316L stainless steel (Azom, 2009)

Grade	Density (kg/m^3)	Elastic Modulus (GPa)	Mean coefficient of Thermal Expansion (µm/m/°C)			Thermal Conductivity (W/m.K)		Specific Heat 0-100°C (J/kg.K)	Elec Resistivity (nΩ.m)
			0-100°C	0-315°C	0-538°C	At 100°C	At 500°C		
316/L	8,000	193	15.9	16.2	17.5	16.3	21.5	500	740

Table.A-2 Grade Specification Comparison of 316L stainless steel (Azom, 2009)

Grade	UNS No	Old British		Euronorm		Swedish SS	Japanese JIS
		BS	En	No.	Name		
316L	S31603	316S11	-	1.4404	X2CrNiMo17-12-2	2348	SUS 316L

A.2.HAAS OM2 SPECIFICATIONS[1]

- The machine is equipped with a 50,000 rpm brushless electric micromotor spindle with 270W power rate.
- The maximum values of feed rate and cutting speed obtained on this micromilling machine are equal to 19.2m/min (757 ipm) and 12.7 m/min (500 ipm).
- The maximum travel distance along X and Z axes are equal to 12” or 305 mm and a travel distance of 10” or 254 mm along Y axis.
- Four-axis machining can be performed using a microrotary table or five-axis machining by installing a microtrunnion table.

---

[1] http://www.haasautomation.com.

Figure A-1. The Haas OM 2 CNC micromachining system (Haas Automation, 2009)

A.3. HAAS VF1 SPECIFICATIONS[2]

- The machine is equipped with a 40- taper cartridge spindle with maximum speed of 7500 rpm driven by a 14.9kW (20-hp) vector dual-drive (Y-Delta) motor.

---

[2] http://www.haasautomation.com.

- The maximum values of feed rate for rapids and cutting obtained on VF-1 machining system equal to 25.4m/min (1,000 ipm) and 16.5 m/min (650 ipm).
- The tool has 508 x 406 x 508 mm (20" x 16" x 20") XYZ travels and is built utilizing all American-made cast-iron components.
- The system has a 20 tool carousel which can be used for multiple machining operations.

Figure A-2. The Haas VF 1 CNC machining system (Haas Automation, 2009)

A.4. KEYENCE LK-G157 LASER SPECIFICATIONS[3]

The main features of this measurement sensor are:

- Sampling speed of 50 KHz
- Measuring range of 150 ±40 mm (5.91 ±1.57")
- Capable of accurately measuring targets rotating or vibrating at high speed.
- Incorporates state of the art algorithms for measuring plastic, transparent or translucent, and metal targets effectively. The LK- Navigator helps to optimize the laser beam to use it effectively based on the measuring surface.

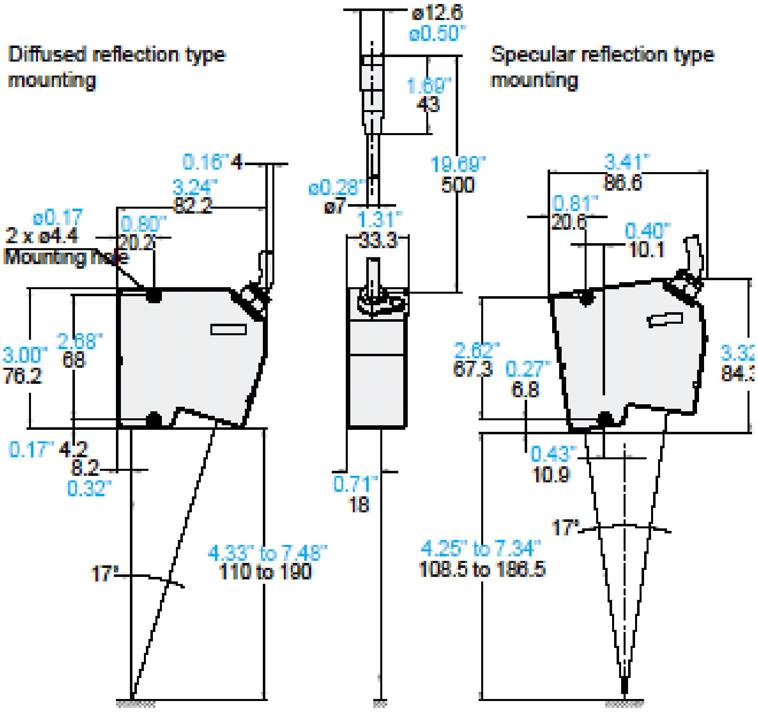

Figure A-3. Different measuring ranges of LK- G 157 laser (Keyence, 2009)

---

[3] http://www.keyence.com.

A.5. UNIST COOLUBRICATOR SYSTEM[4]

- The system is equipped with a 5- 200 pulse/minute pulse generator and a 0.2 drops per cycle to 1.0 drop per cycle liquid metering pump (1 drop equals 0.033cc).
- A brass knurled air metering screw controls the flow of air atomizing out the nozzle which determines the density and distance of the spray.
- The spray output has an included angle of 15-20 degrees depending on the amount of air introduced.

Figure A-4. Unist mist system showing different components (Unist, 2007)

---

[4] http://www.unist.com.

APPENDIX B

MATHEMATICAL CALCULATIONS AND DERIVATIONS

B.1. DERIVATION OF SHEAR AREA

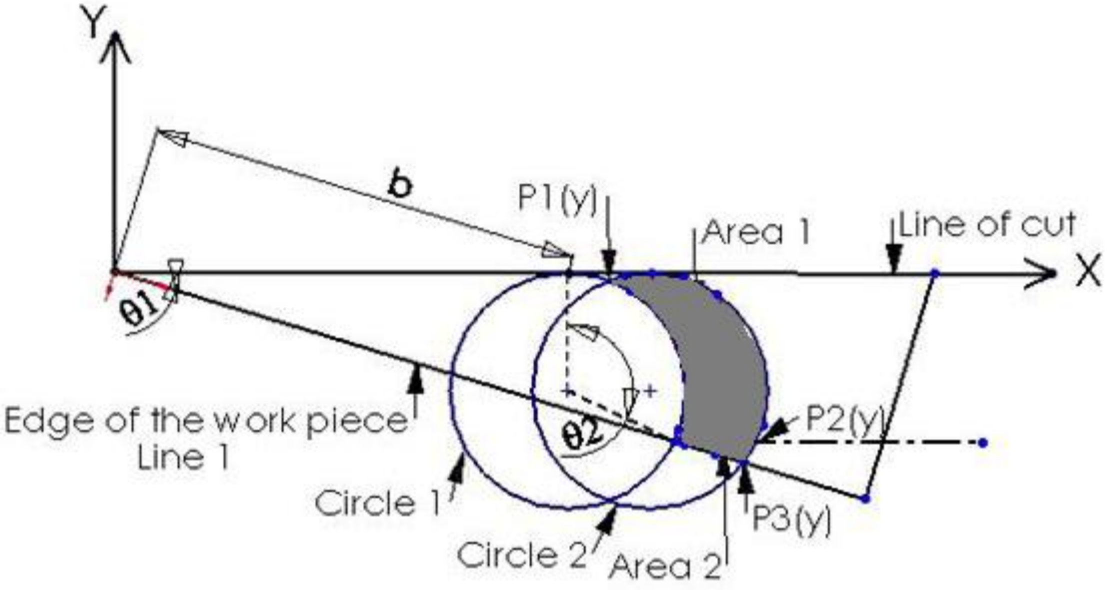

Figure B1. Geometric representation of cutting tool, work piece and line of cut

From the Figure B1, the geometric representation of cutting tool, work piece, line of cut were explained as

Equation of line 1:

$$y = m * x \tag{B1}$$

$$m = -\tan\theta_1 \tag{B2}$$

$$y = -\tan\theta_1 * x \tag{B3}$$

Equation of circle 1:

$$\left(x - b * \sec\theta_1 \right)^2 + (y + R)^2 = R^2 \tag{B4}$$

Equation of circle 2:

$$\left(x - (b * \sec\theta_1 + f_c) \right)^2 + (y + R)^2 = R^2 \tag{B5}$$

where

R = Radius of tool

f_c = Feed per tooth

b = length along line of cut where tool fails

Solving line 1 and circle 1 would help us find the included angle θ_2, which is used to find the arc length cut of circle 1. The arc length of circle 1 multiplied by depth of cut '*h*' would give the shear area A as,

$$A = R * \theta_2 * \left(\frac{\pi}{180}\right) * h \tag{B6}$$

From Figure B1, θ_2 is found equal to is can be defined as

$$\theta_2 = \sin^{-1}\left(\frac{|R+P_1(y)|}{R}\right) + \sin^{-1}\left(\frac{|R+P_2(y)|}{R}\right) \tag{B7}$$

where $P_1(y)$ is the y- coordinate of the point of intersections of circle 1 and circle 2 and $P_2(y)$ and $P_3(y)$ are the y- coordinates of the point of intersection of line 1 with circle 1 and circle 2 respectively. Using the equations (B3), (B4) and (B5), the points $P_1(y)$, $P_2(y)$ and $P_3(y)$ were found equal to,

$$P_1(y) = -R + \sqrt{R^2 - \frac{f_c^2}{4}} \tag{B8}$$

$$P_2(y) = -\left((b * \sec\theta_1) * \cot\theta_1 + R - k_1 \right) * \sin^2\theta_1 \tag{B9}$$

$$P_3(y) = -\left(\left(b * \sec\theta_1 + f_c\right) * \cot\theta_1 + R - k_2\right) * \sin^2\theta_1 \tag{B10}$$

where

$$k_1 = \sqrt{\left((b * \sec\theta_1) * \cot\theta_1 + R\right)^2 - \left((b * \sec\theta_1)^2 * \operatorname{cosec}^2\theta_1\right)} \tag{B11}$$

$$k_2 = \sqrt{\left(\left((b * \sec\theta_1 + f_c) * \cot\theta_1 + R\right)^2 - \left(\left(b * \sec\theta_1 + f_c\right)^2 * \operatorname{cosec}^2\theta_1\right)\right)} \tag{B12}$$

For a given coefficient of friction (μ), friction angle (β) is defined as,

$$\beta = \tan^{-1}(\mu) \tag{B13}$$

The shear plane angle (ϕ) is estimated from the friction angle and the tool rake angle by the Merchant equation (Groover 2004) as,

$$\phi = 45 + \frac{\alpha - \beta}{2} \tag{B14}$$

The above equations (B6) through (B12) were used to find the shear area useful to estimate the shear force and cutting force acting on the tool as,

$$F_s = \tau * R * \theta_2 * h * \left(\frac{\pi}{180}\right) \tag{B15}$$

$$F_c = \tau * R * \theta_2 * h * \left(\frac{\pi}{180}\right) * \left(\frac{\cos(\beta-\alpha)}{\cos(\phi+\beta-\alpha)}\right) \tag{B16}$$

B.1.1 SAMPLE CALCULATION OF SHEAR FORCE AND CUTTING FORCE

For experiment 2, we have from the crash test

$b = 20.9$ mm

$R = 0.02$ in $= 0.508$ mm

$h = 0.0138$ in $= 0.35$ mm

$\theta_1 = \tan^{-1}(0.04/1) = 2.29^{o}$

$f_c = 0.0015$ in $= 0.038$ mm

Therefore,

$b * \sec\theta_1 = 20.917$

$b * \sec\theta_1 + f_c = 20.955$

$(b * \sec\theta_1) * \cot\theta_1 + R = 523.83$

$(b * \sec\theta_1 + f_c) * \cot\theta_1 + R = 524.78$

Therefore, the geometric entities given by equations (B1) through (B3) are,

$y = -0.04 * x$

$(x-20.917)^2+(y+0.508)^2 = 0.508^2$

$(x-20.955)^2+(y+0.508)^2 = 0.508^2$

$k_1 = 9.718$

$k_2 = 9.686$

$P_1(y) = -0.000355$

$P_2(y) = -0.820$

$P_3(y) = -0.822$

$$\sin^{-1}\left(\frac{|R+P_1(y)|}{R}\right)=87.8^\circ$$

$$\sin^{-1}\left(\frac{|R+P_2(y)|}{R}\right)=37.87^\circ$$

$$\theta_2=\sin^{-1}\left(\frac{|R+P_1(y)|}{R}\right)+\sin^{-1}\left(\frac{|R+P_2(y)|}{R}\right)=125.76^\circ$$

Shear strength (τ) = 0.577 * S_u

For 316L stainless steel, S_u=485 MPa;

Therefore, for 316L SS, τ = 0.577 *485MPa = 280 MPa

From equation (B15)

$$F_s=\tau * R * \theta_2 * h * \left(\frac{\pi}{180}\right)$$

Hence shear force (F_s) = 280*0.508 *125.76*(π/180)*0.35 = 109.26N

We have the rake angle of tool (α) = 8°

The crash tests were performed with flood coolant but the analysis was extended to observe the cutting force on the tool for different coolant conditions. The coefficient of friction (μ) values for dry cutting conditions to greasy conditions when machining tungsten carbide tool with 316L SS workpiece were considered. The 'μ' values range from 0.08-0.19 for greasy cutting conditions to dry cutting conditions for machining tungsten carbide tool on 316L SS workpiece (Beardmore 2008).

Table B-1. The friction coefficient (μ) values for steel and tungsten carbide range from 0.08- 0.19 (Beardmore 2008).Considering different values of μ,

μ (=tanβ)	$\phi\ (= 45 + \frac{\alpha - \beta}{2})$	cos (β-α)/cos(φ+β-α)	F_s, N	F_c, N
0.08	46.73	1.37	109.26	149.84
0.09	46.45	1.38		150.62
0.1	46.17	1.39		151.41
0.11	45.88	1.39		152.19
0.12	45.60	1.40		152.96
0.13	45.32	1.41		153.72
0.14	45.04	1.41		154.48
0.15	44.76	1.42		155.24
0.16	44.48	1.43		155.99
0.17	44.20	1.43		156.73
0.18	43.92	1.44		157.47
0.19	43.64	1.45		158.20

Hence the cutting force value for the experiment 2 varies from 150 N to 160 N.

B.2. DERIVATION AND CALCULATIONS FOR FRICTION AREA AND EFFECT OF CUTTER RUNOUT

The friction area was modeled considering the shaded area in Figure (B1) of section B.1. The geometric entities (B3) through (B5) are used to estimate the friction area (A_f) as,

$$\text{Friction Area } (A_f) = \int (x_{circle1} - x_{circle2})\ dy + \int (x_{circle2} - x_{line1})\ dy \qquad \text{(B17)}$$

$$= \int_{P2(y)}^{P1(y)} f_c\, dy + \int_{P3(y)}^{P2(y)} \left(b * \sec\theta_1 + f_c + \sqrt{(R^2 - (y+R)^2)} + y * \cot\theta_1\right) dy \qquad \text{(B18)}$$

The co-ordinates of points $P_1(y)$, $P_2(y)$ and $P_3(y)$ from equations (B8) through (B10) were used to estimate the friction area (A_f) in equation (B14) as,

$$A_f = f_c * \left(-R + \sqrt{R^2 - \frac{f_c^2}{4}} + \left((b * \sec\theta_1 + f_c) * \cot\theta_1 + R - k_2 \right) * \sin^2\theta_1 \right) +$$

$$(b * \sec\theta_1) * (f_c * \cot\theta_1 + k_1 - k_2) * \sin^2\theta_1 + \frac{R^2}{2} (\gamma - \frac{\sin 2\gamma}{2})]_{\gamma_3}^{\gamma_2} + \frac{\cot\theta_1}{2} * \left((P_2(y)^2) - (P_3(y)^2) \right) \qquad \text{(B19)}$$

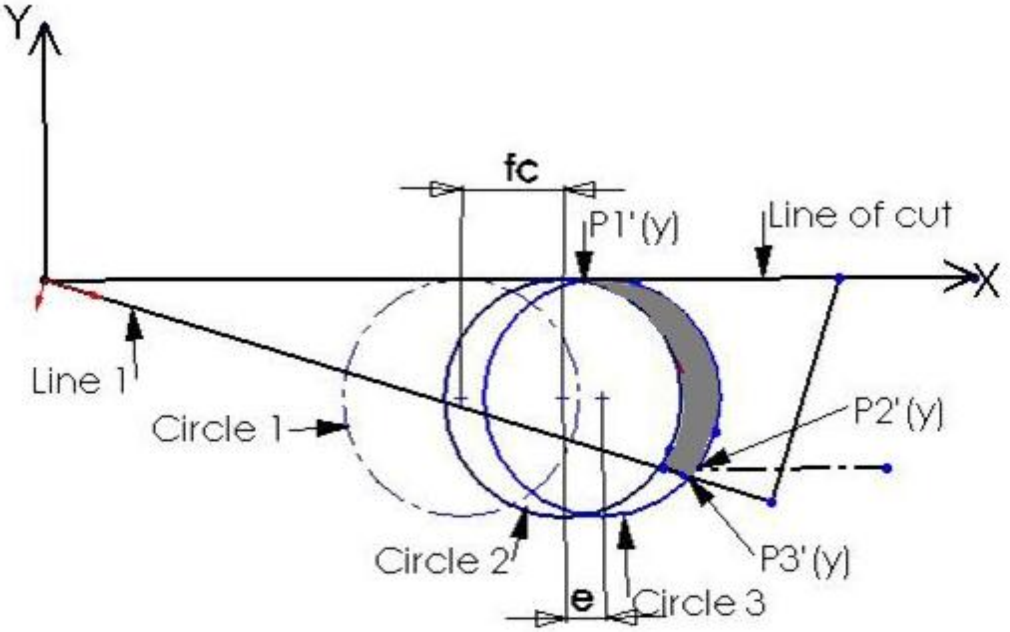

Figure B2. Geometric representation of cutting tool with runout and line of cut

From the Figure B1, the effect of runout on friction area was modeled considering the new position of the tool with the runout in the feed direction, ‘*e*’ along the x-axis. The geometric representation of cutting tool circle 3 with runout ‘*e*’ is,

$$\left(x-(b*\sec\theta_1+f_c+e)\right)^2+(y+R)^2=R^2 \tag{B20}$$

Therefore the additional area due to runout in feed direction is given by A_{r1} as

$$A_{r1}=\int_{P2'(y)}^{P1'(y)} e\ \ dy+\int_{P3'(y)}^{P2'(y)}(b*\sec\theta_1+f_c+e)+\sqrt{(R^2-(y+R)^2)}+\cot\theta_1)\ dy \tag{B21}$$

where $P_1'(y)$ is the y- coordinate of the point of intersections of circle 2 and circle 3 and $P_2'(y)$ and $P_3'(y)$ are the y- coordinates of the point of intersection of line 1 with circle 2 and circle 3 respectively. Using the equations (B3), (B4) and (B15), the points $P_1(y)$, $P_2(y)$ and $P_3(y)$ were found equal to,

$$P_1^{'}(y)= -R+\sqrt{R^2-\frac{e^2}{4}} \tag{B22}$$

$$P_2^{'}(y) = -\Big(\big((b*\sec\theta_1+f_c)*\cot\theta_1+R\big)-k_1^{'}\Big)*\sin^2\theta_1 \tag{B23}$$

$$P_3{'}(y) = -\Big(\big((b*\sec\theta_1+f_c+e)*\cot\theta_1+R\big)-k_2^{'}\Big)*\sin^2\theta_1 \tag{B24}$$

where

$$k_1^{'}=\sqrt{\big((b*\sec\theta_1+f_c)*\cot\theta_1+R\big)^2-((b*\sec\theta_1+f_c)^2*\operatorname{cosec}^2\theta_1)} \tag{B25}$$

$$k_2^{'}=\sqrt{\big((b*\sec\theta_1+f_c+e)*\cot\theta_1+R\big)^2-((b*\sec\theta_1+f_c+e)^2*\operatorname{cosec}^2\theta_1)} \tag{B26}$$

Hence (B21) was obtained from equations (B22) through (B26) as,

$$A_{r1}= e*\left(-R+\sqrt{R^2-\frac{e^2}{4}}+\Big((b*\sec\theta_1+f_c+e)*\cot\theta_1+R-k_2^{'}\Big)*\sin^2\theta_1\right)+ (b*\sec\theta_1+f_c)*\big(e*\cot\theta_1+k_1^{'}-k_2^{'}\big)*\sin^2\theta_1+\frac{R^2}{2}\left(\gamma^{'}-\frac{\sin 2\gamma'}{2}\right)_{\gamma_3'}^{\gamma_2'}+\frac{\cot\theta_1}{2}*\Big((P_2{'}(y)^2)-(P_3{'}(y)^2)\Big) \tag{B27}$$

The shaded area in Figure 19 enclosed between circle 2 and circle 4 is the as the additional area due to cutter runout '*e*' perpendicular to feed direction. Hence for this position of the cutting tool, the additional area of cut due to runout in the direction of feed can be modeled by the method used in the sections 4.2 and 4.2.1.

Equation of circle 4 derived by including the runout distance '*e*' along the y- axis is,

$$\big(x-(b*\sec\theta_1+f_c)\big)^2+(y+R+e)^2=R^2 \tag{B28}$$

From equations (B5) and (B23), the friction area A_{r2} was estimated as,

$$A_{r2}=\int (y_{circle2}-y_{circle4})\ dx \tag{B29}$$

$$=\int_{P_4(x)}^{P_5(x)} e\ dx \tag{B30}$$

where $P_4(x)$ and $P_5(x)$ are the X- coordinates of intersections of circles 2 and 4 and are obtained from equation (B5) and (B23) as

$$P_4(x)=b^*\sec\theta_1+f_c-\sqrt{R^2-\frac{e^2}{4}} \tag{B31}$$

$$P_5(x)=b^*\sec\theta_1+f_c+\sqrt{R^2-\frac{e^2}{4}} \tag{B32}$$

From equations (B25) through (B27), the additional friction area of cut due to cutter runout (*e*) in the direction perpendicular to feed direction, A_{r2}, was defined as,

$$A_{r2}=2^*e^*\sqrt{R^2-\frac{e^2}{4}} \tag{B33}$$

B.2.1 EFFECT OF CUTTER RUNOUT ON CUTTING FORCE

From the Figure B1, the effect of runout on cutting force was calculated. The new position of circle 1 and circle 3 are considered to include the effect of cutter runout (*e*) in feed direction.

From equation (B2), the new position of circle 1 with runout ‘*e*’, is

$$\left(x-(b*\sec\theta_1+e)\right)^2+(y+R)^2=R^2 \tag{B34}$$

And from equation (B20) we have,

$$\left(x-(b*\sec\theta_1+f_c+e)\right)^2+(y+R)^2=R^2 \tag{B20}$$

Therefore the included angle

$$\theta_{2e}=\sin^{-1}\left(\frac{|R+P_1(y)|}{R}\right)+\sin^{-1}\left(\frac{|R+P_2''(y)|}{R}\right) \tag{B34}$$

where $P_1(y)$is obtained from equation (B8)

$$P_2''(y)=-\left(\left((b*\sec\theta_1+e)*\cot\theta_1+R\right)-k_1''\right)*\sin^2\theta_1 \tag{B35}$$

$$k_1''=\sqrt{\left((b*\sec\theta_1+e)*\cot\theta_1+R\right)^2-((b*\sec\theta_1+e)^2*\mathrm{cosec}^2\theta_1)} \tag{B36}$$

Hence cutting force considering runout e in direction of feed was derived as,

$$F_{ce}=\tau*R*\theta_{2e}*h*\left(\frac{\pi}{180}\right)*\left(\frac{\cos(\beta-\alpha)}{\cos(\phi+\beta-\alpha)}\right) \tag{B37}$$

B.2.2 SAMPLE CALCULATION FOR FRICTION AREA (A_f) AND EFFECT OF RUNOUT

From equation (B19)

Friction Area (A_f)

$$= \int_{P2(y)}^{P1(y)} f_c\,dy + \int_{P3(y)}^{P2(y)} (b*\sec\theta_1 + f_c + \sqrt{(R^2-(y+R)^2)} + y*\cot\theta_1)\,dy$$

$$=f_c*\left(P_1(y)-P_3(y)\right) + b*\sec\theta_1*\left(P_2(y)-P_3(y)\right) + \frac{R^2}{2}(\gamma - \frac{\sin2\gamma}{2})]_{\gamma_3}^{\gamma_2} + \frac{\cot\theta_1}{2}*\left(P_2^2(y)-P_3^2(y)\right)$$

For b = 12.7

$b*\sec\theta_1 = 12.710$

$k_1 = 12.720$

$k_2 = 12.719$

$P_1(y) = -0.005717$

$P_2(y) = -0.488$

$P_3(y) = -0.494$

$$\gamma_2 = \sin^{-1}\left(\frac{P_2(y)+R}{R}\right) = 0.040$$

$$\gamma_3 = \sin^{-1}\left(\frac{P_3(y)+R}{R}\right) = 0.028$$

Therefore $A_f = 0.152*(-0.005717+0.488) + 12.710*(-0.488+0.494) + (0.508)^2*(0.00004) + 12.503*(0.488^2-0.494^2)$

$A_f = 0.077\ \text{mm}^2$

Hence the friction area can be calculated by finding the y- coordinates of point of intersection of the geometric entities and using the equation (B19) derived in Appendix B.2.Similar approach can be used for other experiments to find the friction area. The effect of runout ‘*e*’ in feed direction on friction area (A_{r1}) can be similarly calculated. The effect of runout ‘*e*’ perpendicular to feed on friction area can be calculated using equation (B33) as,

$$A_{r2}=2*e*\sqrt{R^2-\frac{e^2}{4}}$$

For R= 0.508 mm, and for runout (*e*) = 10 µm = 0.01 mm we have

$A_{r2} = 2 * 0.01* \sqrt{(0.508^2- (0.01^2/4))} = 0.01016\ \text{mm}^2$

Effect of runout (*e*) on friction area can be easily calculated as above.

B.3.SPECIFIC CUTTING ENERGY ESTIMATION FROM CUTTING FORCE

For experiment 3:

The third experiment is done with same tool and width of cut but depth of cut is increased to 0.0276’

$$u=2*96.60*\frac{\left(\frac{0.114}{0.254}\right)^{0.2}}{0.35*10^{-3}*0.114*10^{-3}}$$

Therefore, u == 44.67 x 10^8 J m^{-3}

APPENDIX C

SPECTRUM ANALYSIS OF RUNOUT DATA USING FAST FOURIER TRANSFORM

C.1 FAST FOURIER TRANSFORM OF TOOL RUNOUT DATA

Fast Fourier Transformation (FFT) has been performed to study the behavior of noise due to electronic system in the tool runout data. The spectrum plots of the runout data were plotted and an adaptive filter was used to study the noise behavior and account for it in the runout values. The tool runout measured at 0 rpm was accounted for noise and was filtered from the runout values at 6000 rpm and 10000 rpm respectively.

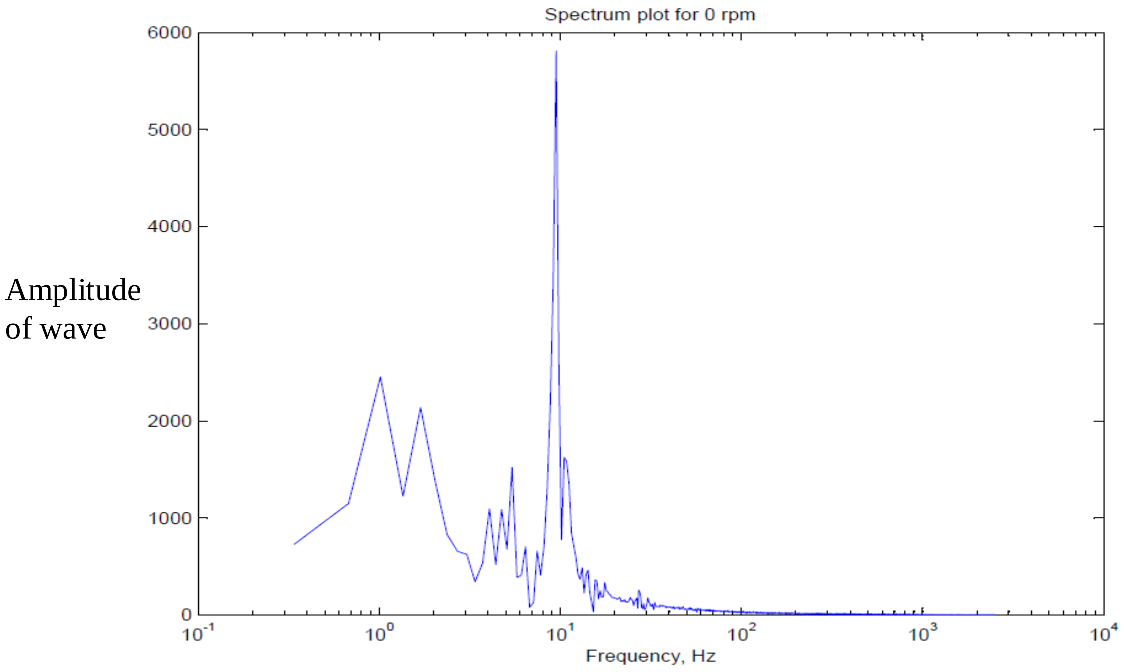

Figure C1. Spectrum plot for 0 rpm (noise)

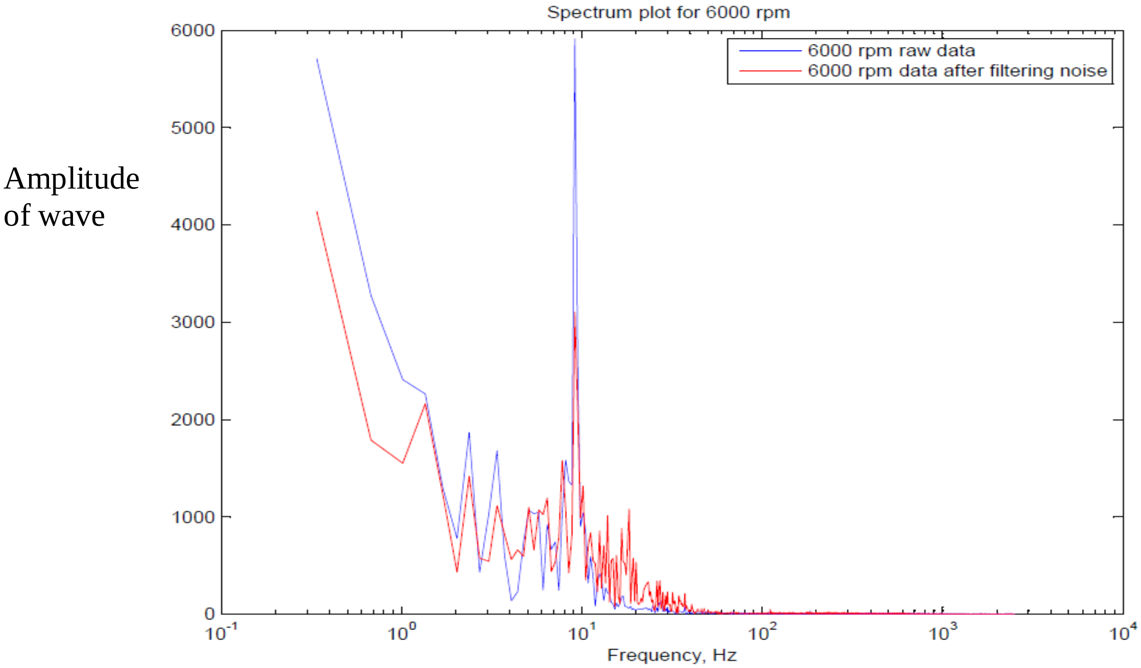

Figure C2.Spectrum plot for 6000 rpm before and after filtering noise

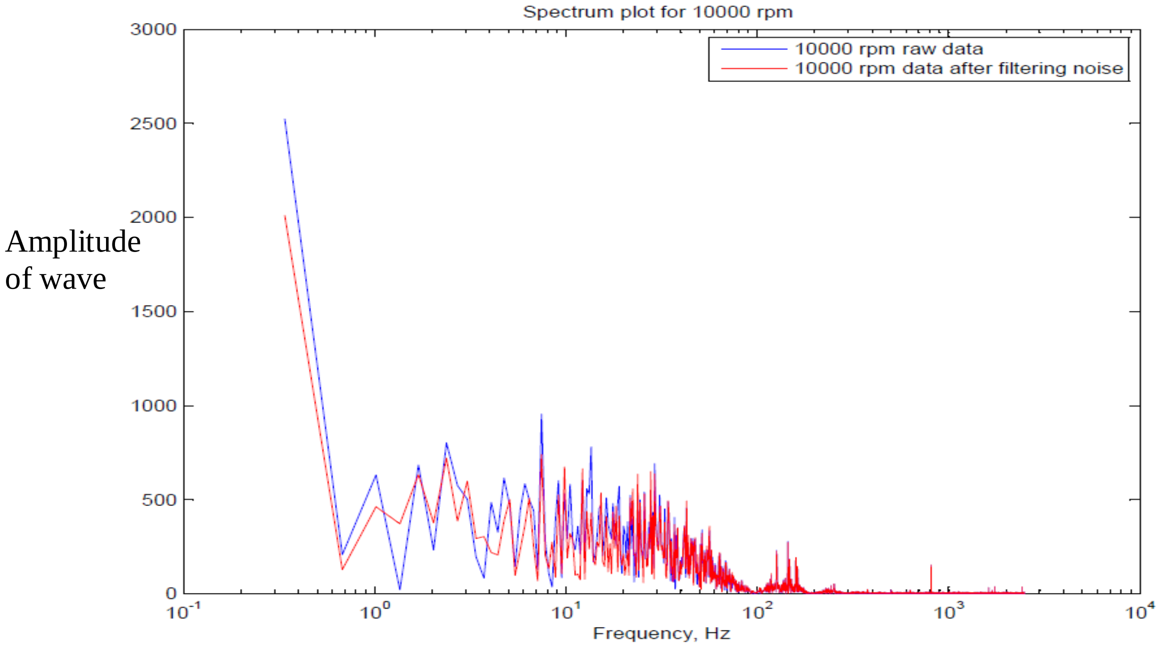

Figure C3. Spectrum plot for 10000 rpm before and after filtering noise

From the data in figures C2 and C3 the time domain plot corresponding to frequencies in the range of 8Hz to 11Hz for 6000 rpm was extracted to estimate the final runout data of the tool without noise. Similarly method was used to extract data for frequencies in the range of 7Hz to 10Hz for 10000 rpm to represent the tool runout without the noise from the electronic system.

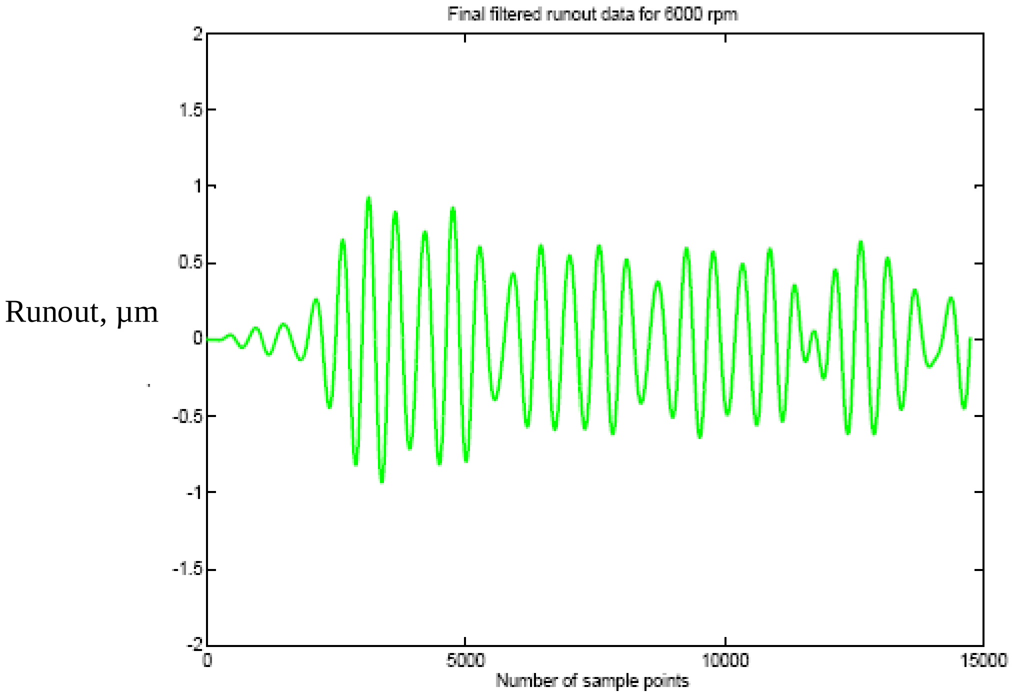

Figure C4. Final runout of tool for spindle speed of 6000 rpm after eliminating drifting of electronic system

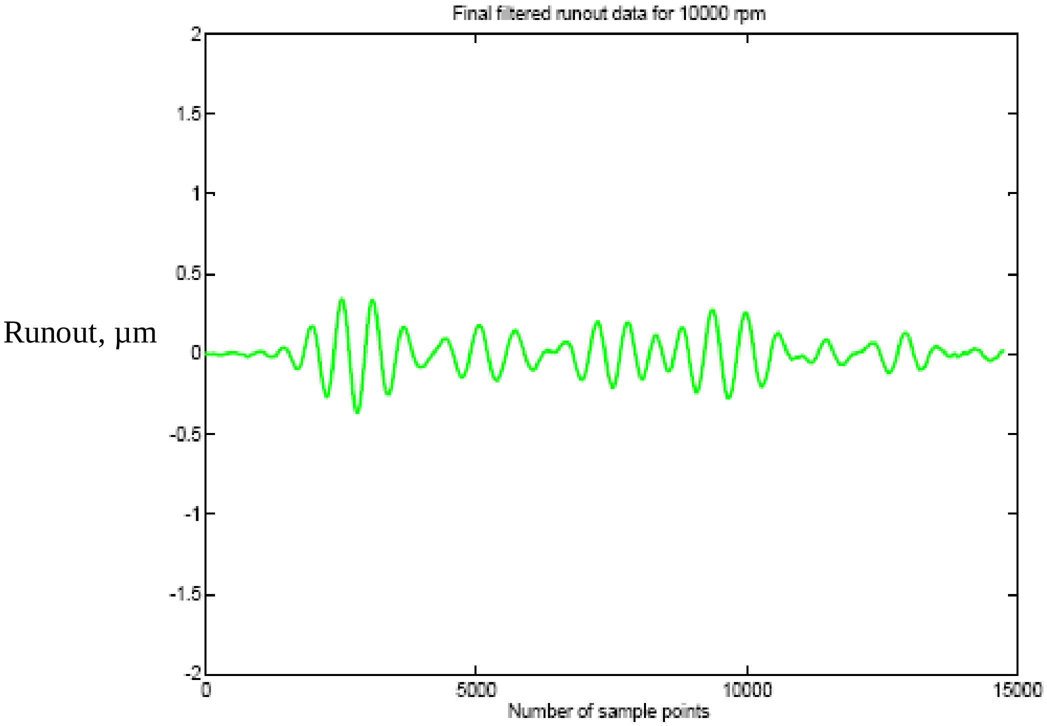

Figure C5. Final runout of tool for spindle speed of 10000 rpm after eliminating drifting of electronic system

From figures C4 and C5 we can clearly see the final tool runout after eliminating the drifting of electronic system is less than 1 µm for 6000 rpm and the runout is less than 0.5 µm for a spindle speed of 10000 rpm.

APPENDIX D

NC PROGRAMS OF CRASH TESTS AND RUNOUT TEST

D.1. NC PROGRAM OF CRASH TEST

```
O03201
( Crash test 1 - 0.0138depth 18ipm feed
38 µm chipload)
( BY FEATURECAM ON 2-20-2009
USING )
( Haas VF Series.CNC
POSTPROCESSOR V9/99 )
N35 G00 G17 G40 G90
( TOOL: T1 = 0.04 dia. 0.04 inch  )
N45 T1 M6
N50 S6000 M03
( OPERATION: FINISH SIDE ON
SIDE1 )
N60 G54 X0.0317 Y-0.0178
N65 G43 H1 Z1.0
N70 Z0.1 M08
N75 G01 Z-0.0138 F9.0
N80 X0.02 Y0.0008 F18.0
N85 X-0.02 Y1.0004
N90 X-0.0098 Y1.0198
N95 G00 Z1.0
( END OF PROGRAM )
N105 G28 G49 G91 Z0. M09
N110 G53 G90 X-20. Y0.
N115 M30
%
```

VITA

Name: Sujeev Chittipolu

Address: C/O Department of Mechanical Engineering,
3123 Texas A&M University,
College Station, TX 77843.

Email Address: sujeevch@gmail.com

Education: B.E., Mechanical Engineering, Osmania University, 2006
M.S., Mechanical Engineering, Texas A&M University, 2009